RESEARCH ARTICLE

Applied Organometallic Chemistry WILEY

Experimental and theoretical studies of new Co(III) complexes of hydrazide derivatives proposed as multi-target inhibitors of SARS-CoV-2

Sakineh Parvarinezhad[1] | Mehdi Salehi[1] | Maciej Kubicki[2] |
Rahimeh Eshaghi Malekshah[3]

[1]Department of Chemistry, Faculty of Science, Semnan University, Semnan, Iran

[2]Department of Chemistry, Adam Mickiewicz University, Poznan, Poland

[3]Medical Biomaterial Research Centre (MBRC), Tehran University of Medical Sciences, Tehran, Iran

Correspondence
Mehdi Salehi, Department of Chemistry, Faculty of Science, Semnan University, PO Box 35195-363, Semnan, Iran.
Email: msalehi@semnan.ac.ir

Cobalt(III) complexes with Schiff base ligands derived from hydrazone, (**HL^1** = (*E*)-*N′*-(3,5-dichloro-2-hydroxybenzylidene)-4-hydroxybenzohydrazide, **HL^2** = (*E*)-*N′*-(3,5-dichloro-2-hydroxybenzylidene)-4-hydroxybenzohydrazide (3,5-dibromo-2-hydroxybenzylidene), and **HL^3** = (*E*)-4-hydroxy-*N′*-(2-hydroxy-3-ethoxybenzylidene)benzohydrazide), were synthesized and characterized by elemental analysis, Fourier transform infrared (FT-IR) spectroscopy, UV–Vis spectroscopy, and cyclic voltammetry. X-ray diffraction was used to determine the single crystal structure of the complex (**1**). Co(III) was formed in a distorted, very regular octahedral coordination in this complex; three pyridine moieties complete this geometry. Schiff base complexes' redox behaviors are represented by irreversible (**1**), quasi-reversible (**2**), and quasi-reversible (**3**) voltammograms. A density functional theory (DFT)/B3LYP method was used to optimize cobalt complexes with a base set of 6-311G. Furthermore, fragments occupying the highest occupied molecular orbital (HOMO) and lowest unoccupied molecular orbital (LUMO) were investigated at the same theoretical level. Quantum theory of atoms in molecules (QTAIM) computations were also done to study the coordination bonds and non-covalent interactions in the investigated structures. Hirshfeld surface analysis was used to investigate the nature and types of intermolecular exchanges in the crystal structure of the complex (**1**). The capacity of cobalt complexes to bind to the major protease SARS-CoV-2 and the molecular targets of human angiotensin-converting enzyme-2 (ACE-2) was investigated using molecular docking. The molecular simulation methods used to assess the probable binding states of cobalt complexes revealed that all three complexes were stabilized in the active envelope of the enzyme by making distinct interactions with critical amino acid residues. Interestingly, compound (**2**) performed better with both molecular targets and the total energy of the system than the other complexes.

KEYWORDS
4-hydroxybenzohhydrazide, Co(III) complex, electrochemical properties, theoretical study, X-ray crystallography

1 | INTRODUCTION

Multidentate Schiff base ligands and their metal complexes have been regarded as attractive in various sectors due to their wide range of uses.[1] It is critical to research drug stability, especially physicochemical stability, to develop an alternate strategy for increasing medication stability by altering the structural features of the molecules.[2] Hydrazone molecules and their derivatives are known as the most important stereochemical models due to their flexibility and capacity to form stable complexes. At the active sites of some metallobiomolecules, nitrogen and oxygen atoms link them to metal ions.[3] Therefore, numerous researchers[4–8] have focused their attention on investigating these compounds. Furthermore, the study of hydrazones is important due to their diverse structural variations and wide range of applications in biological and chemical fields,[9] including anti-tuberculosis,[10] antibacterial,[11] anti-cancer,[12] cytotoxic,[13] antioxidant,[14] anti-inflammatory,[15] and anti-fungal activity.[16] There have only been a small number of crystalline structures of benzohydrazide derivatives described.[17–26] It has been discovered that copper and cobalt complexes have a variety of biological functions, such as protein and DNA binding.[27,28] The bioinorganic chemistry of copper and cobalt complexes has grown fast in recent years. Additionally, these derivatives play a significant role in modifying electronic structures.[29] Researchers have been particularly interested in the catalytic interaction between Cu(II) and Co(III) Schiff base complexes, which has been one of their research subjects. It has been suggested that Co(II) complexes with Schiff base ligands may be among the first carriers of dioxygen.[30] Three axial ligands generate typical cobalt complexes (III) Schiff base ligands of three dentate to complete the six coordinates of the cobalt atom. In addition to cobalt, axial ligands include pyridine and its derivatives, morpholine, thiocyanate anion, imidazoles, and other compounds. The axial ligands greatly influence the cobalt complexes' characteristics.[31–34] The synthesis of cobalt complexes as anti-cancer treatments is currently being studied by many researchers.[35–37] Metal ions such as vanadium (V), palladium (Pd), palladium (Pt), cobalt (Co), nickel (Ni), and copper (Cu) have shown significant biological activity.[38–42] According to research in this field,[43–47] many Schiff base compounds have been demonstrated to enhance anti-cancer and bioactive properties when they are complexed with various metal ions. Cobalt(III) complexes are widely regarded as the most promising anti-cancer agents currently available. We describe the preparation, structural properties, and biological evaluation of mononuclear Co(III) Schiff base complexes using the NO-type ligands shown in Scheme 1. The goal of this study was to investigate various structural, spectroscopic, and electronic properties using density functional theory (DFT), molecular
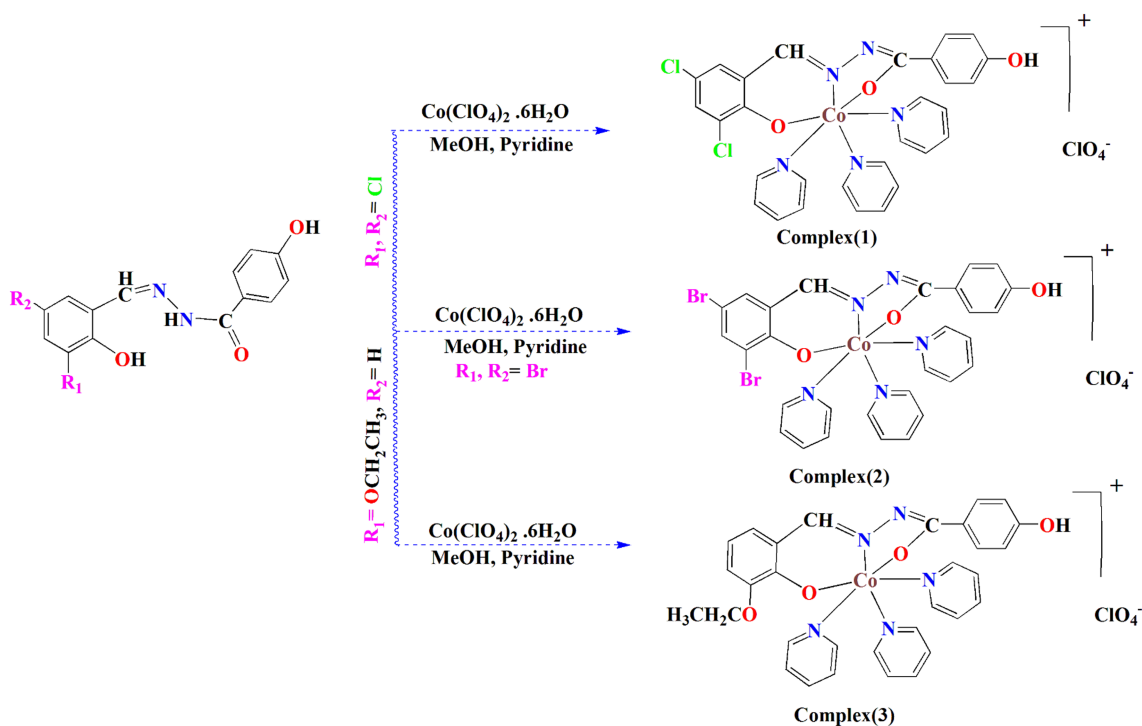
SCHEME 1 Synthetic route for the preparation of the complexes (**1–3**)

electrostatic potential (MEP), and quantum theory of atoms in molecules (QTAIM), as well as intermolecular interactions using Hirshfeld analysis to facilitate and develop their applications. The interactions of the SARS-CoV-2 major protease and human angiotensin-converting enzyme-2 (ACE-2) receptors were also studied using molecular docking.

2 | MATERIALS AND METHODS

All chemicals and solvents were of the highest purity and used as received. The Fourier transform infrared (FT-IR) spectrum of the compounds was recorded in 4000–400 cm^{-1} as KBr pellets on a SHIMADZU FT-IR instrument. UV–Vis spectrum was performed on UV-1650 PC SHIMADZU spectrophotometer in dimethyl sulfoxide (DMSO) solutions. Electrochemical experiments were performed on a Metrohm 757 VA Computrace instrument in a DMSO solution at room temperature. X-ray diffraction (XRD) measurements of the samples were made on a Rigaku Xcalibur four-circle diffractometer. Elemental analysis was performed using Elementar Vario CHNSO and PerkinElmerer device. Hirshfeld surface (HS) analyses were done by the CrystalExplorer Hirshfeld package. All computations were done by DFT in the Gaussian 09 software package. AIM2000 software was used to apply the QTAIM theory to obtain the topology properties of electron density distribution ($\rho(r)$), for example, critical points and Laplacian ($\nabla^2\rho(r)$). The molecular docking was performed by Molegro Virtual Docker (MVD), Molegro Molecular Viewer (MMV), and the Discovery Studio 2020 Client software package.

2.1 | Synthesis

2.1.1 | Preparation of ligand (HL$^{1-3}$)

Schiff base ligands (HL^1–HL^3) were synthesized by reacting 4-hydroxybenzohydrazide and 3,5-dichloro-2-hydroxybenzaldehyde or 3,5-dibromo-2-hydroxybenzaldehyde/3-ethoxy-2-hydroxybenzaldehyde, respectively.[48–50]

(HL^1): Yellow crystals. Yield: 68%. Mol.Wt: 325.15 g mol^{-1}. Anal. Calc. for C$_{14}$H$_{10}$Cl$_2$N$_2$O$_3$: C, 51.72; H, 3.10; N, 8.62%; found: C, 51.36; H, 2.97; N, 8.13%. FT-IR: ν_{max} cm^{-1} (KBr): 3560, 3423 (ν_{O-H}), 3236 (ν_{N-H}), 3193, 3061, 2934 and 2832 (ν_{C-H}), 1647 ($\nu_{C=O}$), 1606 ($\nu_{C=N}$), 1249 (ν_{C-O}). UV–Vis: λ_{max} (nm) (ε, M^{-1} cm^{-1}) (DMSO): 234 (198,000), 278 (89,000), 342 (24,000).

(HL^2): Yellow crystals. Yield: 74%. Mol.Wt: 414.05 g mol^{-1}. Anal. Calc. for C$_{14}$H$_{10}$Br$_2$N$_2$O$_3$: C, 40.61; H, 2.43; N, 6.77%; found: C, 39.98; H, 2.21; N, 6.55%. FT-IR: ν_{max} cm^{-1} (KBr): 3469, 3461 (ν_{O-H}), 3224, 3202 (ν_{N-H}), 3193, 3061, 2934 and 2832 (ν_{C-H}), 1647 ($\nu_{C=O}$), 1606 ($\nu_{C=N}$), 1301 (ν_{C-O}). UV-Vis: λ_{max} (nm) (ε, M^{-1} cm^{-1}) (DMSO): 240 (142,000), 248 (39,000), 263 (42,000), 282 (28,000), 385 (17,000).

(HL^3): Yellow crystals. Yield: 82%. Mol.Wt: 300.31 g mol^{-1}. Anal. Calc. for C$_{16}$H$_{16}$N$_2$O$_4$: C, 63.99; H, 5.37; N, 9.33%; found: C, 63.37; H, 5.12; N, 9.07%. FT-IR: ν_{max} cm^{-1} (KBr): 3500, 3300 (ν_{O-H}), 3208 (ν_{N-H}), 3190, 3058, 2933 and 2832 (ν_{C-H}), 1654 ($\nu_{C=O}$), 1598 ($\nu_{C=N}$), 1271 (ν_{C-O}). UV-Vis: λ_{max} (nm) (ε, M^{-1} cm^{-1}) (DMSO): 238 (50,000), 300 (161,000), 378 (36,000).

2.1.2 | Synthesis of [Co^{III}(HL^1)(py)$_3$]ClO$_4$ (1)

In a typical experiment, a stirring solution of HL^1 (5 mmol, 1.6 g) in 10 ml methanol was added an equimolar amount of Co(ClO$_4$)$_2$·6H$_2$O (5 mmol, 1.8 g). Due to the formation of the complex, a bright red solution was obtained immediately. After half an hour, 1 ml of pyridine was added to the reflux solution, and the solution was stirred for 15 h to obtain a dark red solution. Brown crystals suitable for X-ray analysis were obtained by slow evaporation of the methanol solution after 11 days.

The single crystal obtained from this synthesis was filtered from the solution by vacuum.

Brown crystals. Yield: 86%. Mol.Wt: 718.80 g mol%$^{-1}$. Anal. Calc. for C$_{34}$H$_{35}$Cl$_3$CoN$_5$O$_7$: C, 51.63; H, 4.46; N, 8.85%; found: C, 51.26; H, 4.30; N, 8.32%. FT-IR: (KBr, cm^{-1}): 3384 (ν_{O-H}), 3051, 2923, 2752 (ν_{C-H}), 1610 ($\nu_{C=N}$), 1593 ($\nu_{C=C}$), 1346, 1278 (ν_{C-O}), 646–763 (ν_{M-O}), 516–622 (ν_{M-N}). UV–Vis: λ_{max} (nm) (ε, M^{-1} cm^{-1}) (DMSO): 292 (135,000), 335 (63,000), 349 (74,000), 400 (42,000), 427 (4000), 545 (370).

2.1.3 | Synthesis of [Co^{III}(HL^2)(py)$_3$]ClO$_4$ (2)

Complex (2) was synthesized similarly to the complex (1) method, except that HL^2 was used instead of HL^1.

Brown crystals. Yield: 87%. Mol.Wt: 879.87 g mol%$^{-1}$. Anal. Calc. for C$_{34}$H$_{35}$ClCo Br$_2$N$_5$O$_7$: C, 46.41; H, 4.01; N, 7.96%; found: C, 45.98; H, 3.83; N, 7.47%. FT-IR: (KBr, cm^{-1}): 3259 (ν_{O-H}), 3108, 2953, 2923 (ν_{C-H}), 1608 ($\nu_{C=N}$), 1585 ($\nu_{C=C}$), 1373, 1344, 1309 (ν_{C-O}), 620–757 (ν_{M-O}), 532 (ν_{M-N}). UV–Vis: λ_{max} (nm) (ε, M^{-1} cm^{-1}) (DMSO): 290 (190,000), 328 (80,000), 346 (93,000), 392 (42,000), 415 (41,000), 614 (480).

2.1.4 | Synthesis of [Co^{III}(HL^3)(py)$_3$]ClO$_4$ (3)

Complex (**3**) was synthesized similarly to the complex (**1**) method, except that **HL^3** was used instead of **HL^1**.

Brown crystals. Yield: 79%. Mol.Wt: 766.13 g mol%$^{-1}$. Anal. Calc. for C$_{36}$H$_{41}$ClCo N$_5$O$_8$: C, 56.44; H, 5.39; N, 9.14%; found: C, 55.46; H, 5.11; N, 9.01%. FT-IR: (KBr, cm^{-1}): 3289 (υ_{O-H}), 2954, 2923, 2752 (υ_{C-H}), 1606 ($\upsilon_{C=N}$), 1593 ($\upsilon_{C=C}$), 1390, 1361 (υ_{C-O}), 665–736 (υ_{M-O}), 642 (υ_{M-N}). UV–Vis: λ_{max} (nm) (ε, M^{-1} cm^{-1}) (DMSO): 278 (138,000), 336 (40,000), 412 (30,000), 434 (31,000), 668 (300).

2.2 | Crystal structure determination

Diffraction data were collected by the ω-scan technique, at 130(1) K, on Rigaku SuperNova four-circle diffractometer with Atlas CCD detector, equipped with mirror-monochromatized CuK$_\alpha$ radiation source ($\lambda = 1.54178$ Å). The data were corrected for Lorentz-polarization and absorption effects.[51] The structures were solved with SHELXT[52] and refined with the full-matrix least-squares procedure on F^2 by SHELXL-2013.[53] All non-hydrogen atoms were refined anisotropically; hydrogen atoms were placed in idealized positions and refined as a "riding model" with isotropic displacement parameters set at 1.2 (1.5 for methyl groups) times the U$_{eq}$ of appropriate carrier atoms. Table 1 lists the relevant crystal data and refinement details.

2.3 | Cyclic voltammetry

The oxidation and reduction potential values of cobalt complexes and the issue of reversibility or irreversibility in the metal complexes were investigated using cyclic voltammetry. For this purpose, a 10^{-3} M solution of the desired complex solvent was prepared in DMSO. The combination of tetrabutylammonium hexafluorophosphate (TBAH) with a concentration of 0.1 M was used as a supporting electrolyte. Electrochemical studies were performed at a speed of 100 mV s^{-1}. Glass carbon was utilized as the working electrode, Ag/AgCl was used as the reference electrode, and Pt was used as the auxiliary electrode. Alumina powder was employed as an electrode polish. The solutions were deoxygenated with Ar gas for 15 min, and the electrochemical potentials were calibrated against internal Fc$^{+/o}$ (E^0 = 0.45 V). It should be noted that the value of E$_{1/2}$ has been corrected compared with E$_{1/2}$ of the Fc/Fc$^+$ pair.

TABLE 1 Crystal data and refinement details

Formula	C$_{29}$H$_{23}$Cl$_2$CoN$_5$O$_3$$^+$·ClO$_4$$^-$
Formula weight	718.80/c
Crystal system	Monoclinic
Space group	$P2_1/c$
a (Å)	15.1195(3)
b (Å)	9.2995(2)
c (Å)	21.0390(4)
β (°)	99.648(2)
V (Å^3)	2916.32(10)
Z	4
D$_x$ (g cm^{-3})	1.637
F(000)	1464
μ (mm^{-1})	7.645
Reflections:	
Collected	13,424
Unique (R$_{int}$)	5977 (0.034)
With I > 2σ(I)	5173
R(F) [I > 2σ(I)]	0.0390
wR(F^2) [I > 2σ(I)]	0.0972
R(F) [all data]	0.0470
wR(F^2) [all data]	0.1025
Goodness of fit	1.028
max/min Δρ (e·Å^{-3})	0.35/−0.62
CCDC number	2168778

2.4 | Computational details

Computational chemistry studies based on DFT were performed using GaussView 5.0.8 and the Gaussian 09 package.[54–56] All calculations used the B3LYP function, base set 6-311G, for cobalt complexes. Natural bond orbital (NBO) analysis was used to study the electronic aspects of the complex's structures.[57] Also, the topological properties at critical points were analyzed using the QTAIM[58] and the AIM2000 program. MEP calculations were investigated using GaussView 5.0.8 and Gaussian 09[54–56] density and charge determined at the same level of theory.

2.5 | HS analysis

An HS analysis is one of the suitable and available graphical tools to study different types of intermolecular interactions in the structure. This analysis uses the drawing of colored 3D surfaces based on the electron density around the molecule's atoms; it allows the qualitative and quantitative investigation of close intermolecular contacts in molecular structures. CrystalExplorer 17.5 software is

used to draw these levels.[59] HS analysis is often defined in terms of the normalized form of distance (d_{norm}) based on the distances d_i and d_e (Equation 1). In this equation, r_i^{vdw} and r_e^{vdw} are the van der Waals radii of internal and external atoms.

$$d_{norm} = \frac{d_i - r_i^{vdw}}{r_i^{vdw}} + \frac{d_e - r_e^{vdw}}{r_e^{vdw}} \qquad (1)$$

In addition, the distances from the surface to the nearest atom inside (d_i) or outside the surface (d_e), the shape index, the curvedness, and the information obtained from these three-dimensional surfaces are presented in the form of two-dimensional fingerprint diagrams. The d_{norm} HSs are drawn in three colors: red, white, and blue, with red representing strong interactions (interactions with atomic distances are smaller than the sum of the van der Waals radii of the two interacting atoms), white representing moderate interactions (interactions with atomic distances are equal to the sum of the van der Waals radii of the two interacting atoms), and blue indicating the weak interactions (interactions with the atomic distances are greater than the sum of the van der Waals radii of the two interacting atoms). Fingerprint diagrams are also drawn based on d_i and d_e distances and provide the percentage of participation of various intermolecular interactions.[54–56,60]

2.6 | Molecular docking method

Protein–ligand interactions between the studied complexes and the target proteins 6Y2F and 6M0J related to the SARS-CoV-2 main protease and human ACE-2 were determined by molecular docking AutoDock Vina. A protein database (6M0J, 6Y2F. PDB http://www.rcsb.org/pdb) was used to initiate the binding process.[61] Water molecules, heteroatoms, and structure ligands 6M0J and 6Y2F were removed using Discovery Studio software.[60,62] The structures of the cobalt complexes were optimized by DFT/B3LYP/6-311G and used as the input file of the dock software.

3 | RESULTS AND DISCUSSION

3.1 | Synthesis

In this study, three new complexes of hydrazide derivatives were synthesized, which may be a key reaction for developing new bioactive heterocyclic drugs in the future.

TABLE 2 Relevant geometrical data for **1**, with s.u.'s in parentheses

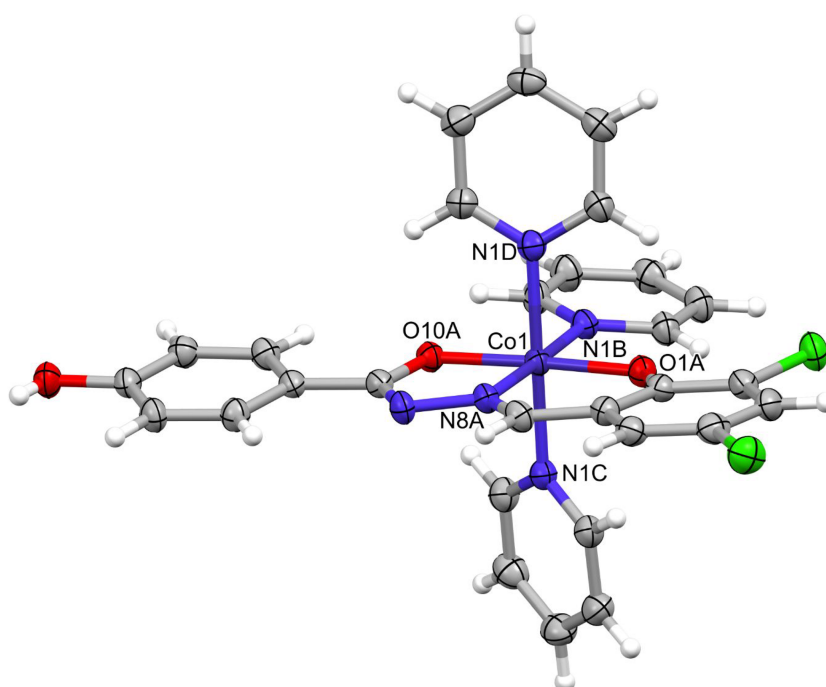|			
Co1-O1A	1.8727(16)	Co1-N1B	1.985(2)
Co1-N8A	1.878(2)	Co1-N1C	1.975(2)
Co1-O10A	1.8811(16)	Co1-N1D	1.998(2)
C1A-O1A	1.308(3)	C10A-O10A	1.307(3)
O1A-Co1-O10A	176.76(7)	N8A-Co1-N1B	176.18(8)
N1C-Co1-N1D	176.53(8)		
C7A-N8A-N9A	117.8(2)	C2B-N1B-C6B	118.8(2)
C2C-N1C-C6C	118.2(2)	C2D-N1D-C6D	117.8(2)

FIGURE 1 Perspective view of the complex **1**; ellipsoids are drawn at the 50% probability level; hydrogen atoms are shown as spheres of arbitrary radii.
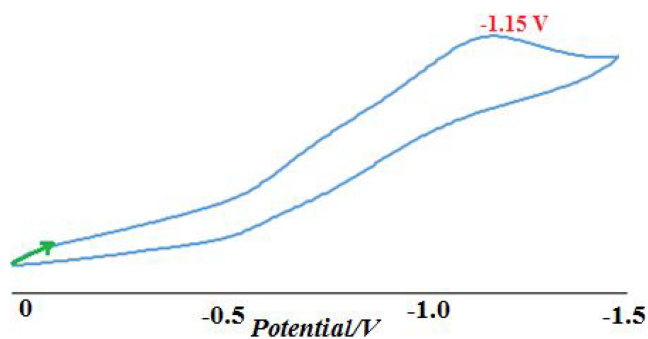
FIGURE 2 Cyclic voltammogram of 10^{-3} mol L^{-1} solutions of Co(III) complex (**1**) in dimethyl sulfoxide (DMSO) solutions containing 0.1 mol L^{-1} tetrabutylammonium hexafluorophosphate (TBAH) and scan rate 100 mV s^{-1}

FIGURE 3 Cyclic voltammogram of 10^{-3} mol L^{-1} solutions of Co(III) complex (**2**) in dimethyl sulfoxide (DMSO) solutions containing 0.1 mol L^{-1} tetrabutylammonium hexafluorophosphate (TBAH) and scan rate 100 mV s^{-1}
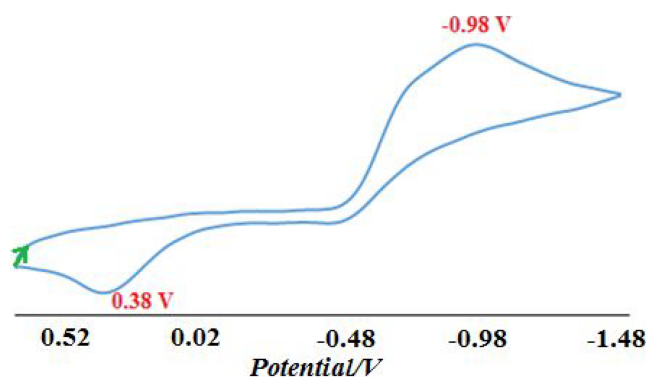
All three complexes were identified using elemental analysis, FT-IR, and UV–Vis spectroscopy techniques. The three-dimensional structures of complex (**1**) were validated by single crystal XRD, and all three structures were optimized and validated by DFT calculations. Computational chemistry was used to predict the complex structures by calculating the vibrational frequency and electron transmissions and comparing the results with the experimental. Also, NBO analysis was performed to investigate hydrogen bonds. Also, HS analysis was done on all three complexes to assess the strength of hydrogen bonds and other intermolecular interactions. Due to the importance of studying molecular docking in the process of drug design and synthesis, the tendency of complexes to bind and interact with molecular targets in the treatment of Covid-19 (SARS-CoV-2 and human ACE-2 enzymes) with protein (PDB ID: 6M0J, 6Y2F) was investigated.
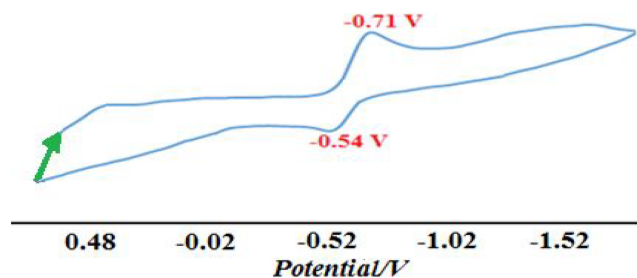

FIGURE 4 Cyclic voltammogram of 10^{-3} mol L^{-1} solutions of Co(III) complex (**3**) in dimethyl sulfoxide (DMSO) solutions containing 0.1 mol L^{-1} tetrabutylammonium hexafluorophosphate (TBAH) and scan rate 100 mV s^{-1}

3.2 | FT-IR spectra of the ligands (HL$^{1-3}$) and complexes (1–3)

The infrared spectra of **HL**$^{1-3}$ ligands and cobalt(III) complexes are presented in Figures S1–S3, respectively. In the **HL**$^{1-3}$ ligands spectrum, bands appear in the regions of 1647, 1647, and 1654 cm^{-1}, respectively, which belong to the stretching vibration $\upsilon_{(C=O)}$. Also, the stretching vibration band $\upsilon_{(C=N)}$ has appeared in areas 1622, 1616, and 1616 cm^{-1}. This area $\upsilon_{(C=N)}$ in the spectrum of complexes (**1–3**) is transferred to lower energies of 1610, 1608, and 1606 cm^{-1}, respectively. Furthermore, in the spectrum of ligands, $\upsilon_{(O-H)}$ bands are observed in the regions of 3400–3500 cm^{-1}, which in the vibrational spectrum of the complexes, the absence of O—H stretching bands in the region indicates the coordination of oxygen to the central metal. In addition, the M—O and M—N stretching bands in the complexes are observed in the lower wavelength range of 646–763 and 516–622 cm^{-1} (for complex (**1**)), 620–757 and 532 cm^{-1} (for complex (**2**)), and 665–736 and 642 cm^{-1} (for complex (**3**)). Moreover, in the free ligands **HL**$^{1-3}$, phenolic C—O stretching vibration bands are assigned in the regions of 1249, 1301, and 1299 cm^{-1}, which are shown in the higher wavenumbers of 1278, 1346 (for complex (**1**)), 1309–1373 (for complex (**2**)), and 1361–1390 cm^{-1} (for complex (**3**)) compared with the stretching vibration band complexes. Also, these results prove the coordination of the (O)$_{\text{2-hydroxy benzaldehyde ring}}$ of the ligand to the cobalt(III) ion.[63–65]

3.3 | Spectroscopic characterizations to be UV–Vis of the ligands (HL$^{1-3}$) and complexes (1–3)

Electron absorption spectra were recorded in DMSO solvent. Figures S4-S6 show the UV–Vis spectrum of the **HL**$^{1-3}$ ligands. In the UV–Vis spectrum, the ligands have

FIGURE 5 Optimized molecular structures of complexes (1–3)

Complex (1)   Complex (2)   Complex (3)
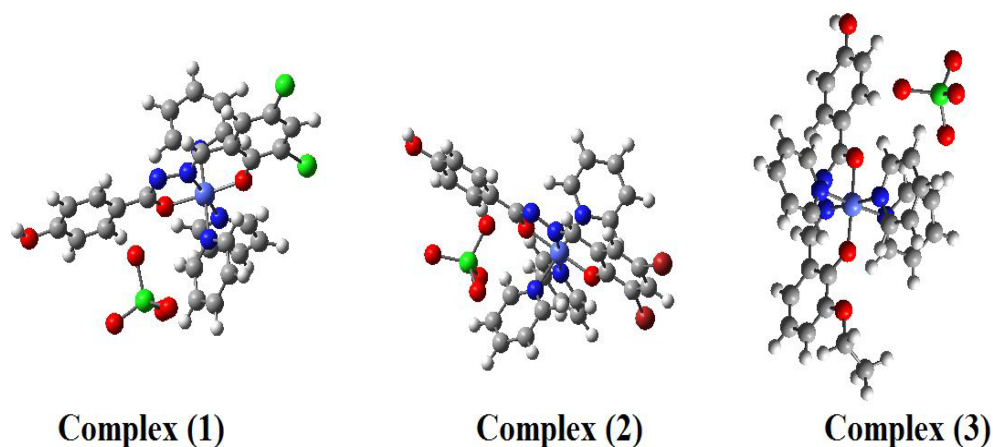
a strong peak of about 234, 240–248, and 238 nm belonging to the $\pi \rightarrow \pi^*$ aromatic ring transitions. The peaks at 278, 263–282, and 300 nm are attributed to the transfer of the $\pi \rightarrow \pi^*$ azomethine group. In addition, the peaks at 342, 385, and 378 nm correspond to the $n \rightarrow \pi^*$ azomethine group. The electron transition spectrum of complexes (1–3) is shown in Figures S4-S6. The spectra of complex electron transitions relative to the ligands showed bands in the higher regions, which include absorption bands in the regions of 335, 349, 400, and 427 nm (for complex (1)), 328, 346, 392, and 415 nm (for complex (2)), and 336, 412, and 434 nm (for complex (3)), which correspond to the intra-ligand transitions of the azomethine group and the metal-to-ligand charge transfer (MLCT) transitions.[63-65] These absorption bands at a high wavelength confirm the coordination of the cobalt(III) ion to the azomethine group (C=N). Also, the wide shoulders observed in the 545, 614, and 668 nm regions are assigned to $d \rightarrow d$ transitions in cobalt complexes (1–3), respectively.[64]

3.4 | Description of the crystal structure

The perspective view of complex 1 is shown in Figure 1; the relevant geometrical data are presented in Table 2.

In the cationic complex molecule, the Co center is six-coordinated (N_2O_4), in slightly distorted octahedral coordination. The almost planar ligand molecule acts as a three-dentated one while three nitrogen atoms from three pyridine molecules are additionally involved in coordination. Such coordination is quite typical for Co complexes. The charge is balanced by the perchlorate anion, hydrogen-bonded with the OH group of the ligand (O···O 2.814(2) Å, H···O 1.98 Å, O—H···O 177°). The details of the intermolecular interactions were studied using the HS method and will be presented further in the text.

3.5 | Electrochemistry

Cycle voltammetry for complexes was recorded in DMSO solution. Figure 2 shows the cyclic voltammeter of complex (1). As shown in Figure 2, the irreversible oxidation process in the −1.15 V region has been attributed to the cathodic voltammogram, and no voltammogram is observed in the anodic region, which is assigned to the reducing process of the transfer Co(III)/Co(II).[64] The complex (2) cycle voltammetry is shown in Figure 3. The oxidation process in areas of −0.98 V is attributed to the cathodic voltammogram, and in areas of 0.38 V is related to the anodic voltammogram, which belongs to the transfer of $Co^{(III)}/Co^{(II)}$ and $Co^{(II)}/Co^{(III)}$, respectively.[64] Figure 4 shows the complex (3) cycle voltammogram. According to the results obtained from the redox process, the potential observed in the cathodic range of −0.71 V to reduce $Co^{(III)}/Co^{(II)}$ and in the range of −0.54 V is also related to the oxidation process of $Co^{(II)}/Co^{(III)}$.[64]

3.6 | Computational chemistry and DFT calculations

3.6.1 | Vibrational analysis

The electronic structures of all three complexes were optimized by the Gauss 09 program in the gas phase, at the level of theory (B3LYP/6-311G). Figure 5 presents the optimized structures of three complexes. A comparison of some theoretical and experimental parameters of the vibrational frequency of the studied complexes is presented in Table 3. The stretching frequencies of the $\nu_{(C—O)}$ bond appeared to be about 1278–1390 cm^{-1} for all three complexes (1–3) in the experimental results, whereas the wavenumbers of the theoretical studies for the Co(III) (1–3) complexes were approximately 1366, 1366, and 1363 cm^{-1}. In addition, the experimental data for the

TABLE 3 The important vibrational frequency of experimental and computational data and vibrational modes using the B3LYP method in the base set (6-311G)

Experimental	Calculated B3LYP/6-311G	Tentative assignment
Complex (1)		
3384	3694	υ(O—H)
3051	3222, 3237, 3245, 3250, 3266, 3270	υ(C—H)$_{Pyridine}$
3968	3202, 3226	υ(C—H)$_{Aldehyde}$
2923	3156	υ(C—H)$_{H—C=N}$
2782	3158, 3209, 3217	υ(C—H)$_{Benzohydrazide}$
1593	1617, 1620, 1642	υ(C=C)
1610	1650	υ(C=N) + υ(C=C)
1346	1366	υ(C=O)$_{Benzohydrazide}$
1278	1291, 1296, 1342	υ(O—C)
1100	1176, 644	υ(O—Cl)
516–622	494, 506, 683	υ(N—Co)
646–763	596, 668, 736	υ(O—Co)
Complex (2)		
3259	3694	υ(O—H)
3108	3222, 3237, 3243, 3248, 3266, 3269	υ(C—H)$_{Pyridine}$
3953	3198, 3222	υ(C—H)$_{Aldehyde}$
2923	3155	υ(C—H)$_{H—C=N}$
2819	3208, 3217	υ(C—H)$_{Benzohydrazide}$
1585	1618, 1642, 1643	υ(C=C)
1608	1650	υ(C=N) + υ(C=C)
1373	1366	υ(C=O)$_{Benzohydrazide}$
1344, 1309	1295, 1341	υ(O—C)
1100	1163, 632	υ(O—Cl)
532	447, 550, 648, 683	υ(N—Co)
620–757	667, 680, 709	υ(O—Co)
Complex (3)		
3289	3695	υ(O—H)
2987	3220, 3234, 3245, 3266, 3268, 3270	υ(C—H)$_{Pyridine}$
2954	3169, 3190, 3209	υ(C—H)$_{Aldehyde}$
2923	3153	υ(C—H)$_{H—C=N}$
2752	3158, 3176, 3216	υ(C—H)$_{Benzohydrazide}$
1591	1606, 1619, 1643	υ(C=C)
1606	1651	υ(C=N) + υ(C=C)
1390	1363	υ(C=O)$_{Benzohydrazide}$
1361	1303	υ(O—C)
1100	1157, 643	υ(O—Cl)
642	458, 495, 515, 541	υ(N—Co)
665–736	649–658	υ(O—Co)

three complexes were observed in the stretching frequencies $\nu_{(C=N)}$ and $\nu_{(C=C)}$ bonds in the areas of 1610 and 1593 (for (**1**)), 1608 and 1585 (for (**2**)), and 1606 and 1591 cm^{-1} (for (**3**)), which are the same areas as the calculated wavenumbers, indicating that the combination of vibrations (υ(C=N) + υ(C=C)) for all three complexes was obtained at about 1650–1642 cm^{-1}. Experimental results for stretching frequencies of the Co—N and Co—O bonds of the complexes were also observed in the regions of 516–763 cm^{-1}, which relates to the calculus wavenumbers of nearly 494–763 cm^{-1} for (**1**), 447–709 cm^{-1} for (**2**), and 458–658 cm^{-1} for (**3**). More information on other vibrational frequencies is summarized in Table 3. The results of these theoretical calculations were well consistent with experimental results.

3.6.2 | UV–Vis spectrum

According to the UV–Vis spectrum, all three complexes in the DMSO solution (Figures S7–S9) were compared with experimental data using the computational chemistry spectrum of electron transfer at the same level of theory. For all three complexes, electron transfer spectra from computational chemistry with a higher adsorption band were detected. The highest adsorption bands of complexes (**1–3**) were detected at wavelengths of 323–367, 334–367, and 344–359 nm, respectively, with energy transfers of 3.862–3.654, 3.864–3.655, and 3.787–3.699 eV, which was attributed to the azomethine group's electron transfer. The experimental spectra of complexes (**1–3**) showed a band at 400–427, 392–415, and 412–434 nm, indicating MLCT and octahedral geometry, respectively. For each of the three complexes (**1–3**), absorption band transitions of about 548, 614, and 668 nm, as well as characteristic bands of computational chemistry of 630, 620, and 714 nm with energy transfers of 1.965, 1.995, and 1.521 eV, were detected, showing d–d transitions. The results reveal that computational chemistry accurately predicted the structure of all three complexes. Also, according to the energy transfer, it can be understood that the quantity of high energy gap shows good consistency as well as excellent chemical strength, and low reactivity.[66,67] Complex (**2**) has a higher energy gap than the other complexes, showing a higher chemical hardness, which will be proved in Section 3.6.3.

3.6.3 | Frontier molecular orbital analysis

Figure 6 shows lowest unoccupied molecular orbital (LUMO) and highest occupied molecular orbital (HOMO) images calculated at the B3LYP/6-311G level of

FIGURE 6 Surface plots of highest occupied molecular orbital (HOMO) and lowest unoccupied molecular orbital (LUMO) for complexes (**1–3**)
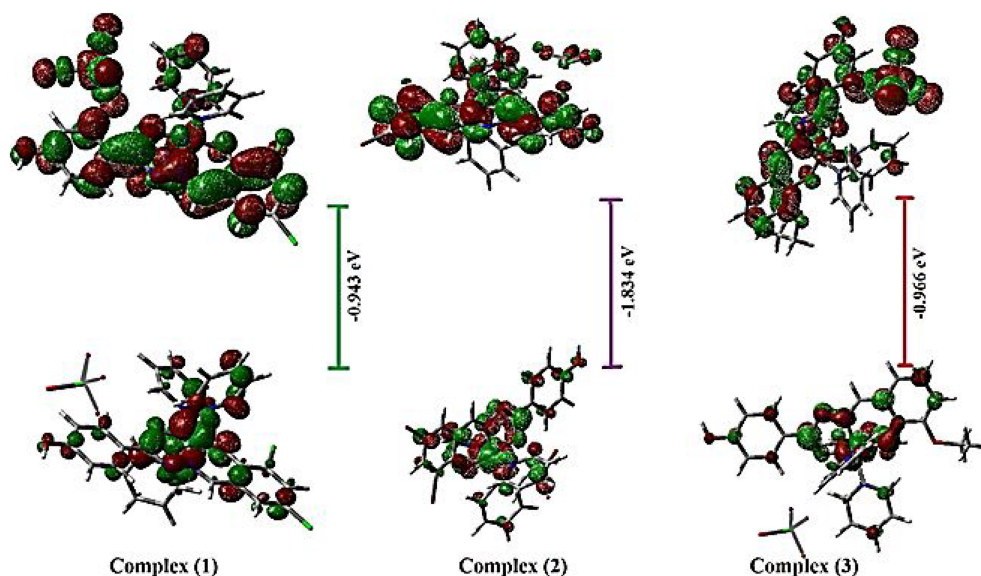

−0.943 eV   −1.834 eV   −0.966 eV

Complex (1)   Complex (2)   Complex (3)

TABLE 4 Calculated global reactivity descriptors of the complexes (**1–3**) at the B3LYP/6-311G level

Parameters	Complex (1)	Complex (2)	Complex (3)
E_{LUMO} (eV)	−4.994	−4.234	−4.980
E_{HOMO} (eV)	−5.937	−6.068	−5.946
$E_{LUMO} - E_{HOMO}$ (eV)	−0.943	−1.834	−0.966
$E_{LUMO} + E_{HOMO}$ (eV)	−10.93	−10.30	−10.92
Electronegativity (χ)	2.732	5.151	5.463
Chemical potential (μ)	−2.732	−5.151	−5.463
Chemical hardness (η)	−0.471	−0.917	−0.483
Softness (S)	−1.060	−0.545	−1.03

Abbreviations: HOMO, highest occupied molecular orbital; LUMO, lowest unoccupied molecular orbital.

theory for all three complexes. HOMO and LUMO energy levels for complexes were −5.937 and −4.994 eV for (**1**), −6.068 and −4.234 eV for (**2**), and −5.946 and −4.980 eV for (**3**), respectively (Table 4). An interesting decision was supplied by the map of frontier molecular orbitals (FMOs). The LUMO value determines the electron-accepting capability (nucleophilicity), whereas the HOMO value is apprehensive about the molecule's nature to donate electrons (electrophilicity).[68] The lesser the LUMO amount, the better the electron acceptor ability.[68] According to the results of Table 4, it is concluded that complex (**1**) has a lower LUMO value than the other complexes. Compared with complex (**2**), the energy difference (ΔE) of complexes (**1** and **3**) is lower relatively (**2** > **3** > **1**), demonstrating that the Co ion has a stronger potential for accepting electrons or donating electrons as an active center, and the biological activity of complexes should be **1** > **3** > **2**.[69] Using the energy of the orbitals, quantum parameters such as reactivity, electronegativity (χ), chemical potential (μ), chemical hardness (η), and

softness (S) can be calculated.[54–56] These parameters were calculated using Equations 2–6, respectively.

$$E_{GAP} = E_{LUMO} - E_{HOMO} \qquad (2)$$

$$\chi = -1/2(E_{LUMO} + E_{HOMO}) \qquad (3)$$

$$\mu = -\chi \qquad (4)$$

$$\eta = 1/2(E_{LUMO} - E_{HOMO}) \qquad (5)$$

$$S = \frac{1}{2\eta} \qquad (6)$$

The calculation's results of quantum parameters for the studied complexes are listed in Table 4. A molecule with a lower (ΔE) between the HOMO and LUMO orbitals has higher polarity and higher chemical reaction and acts as a soft molecule. According to the values calculated
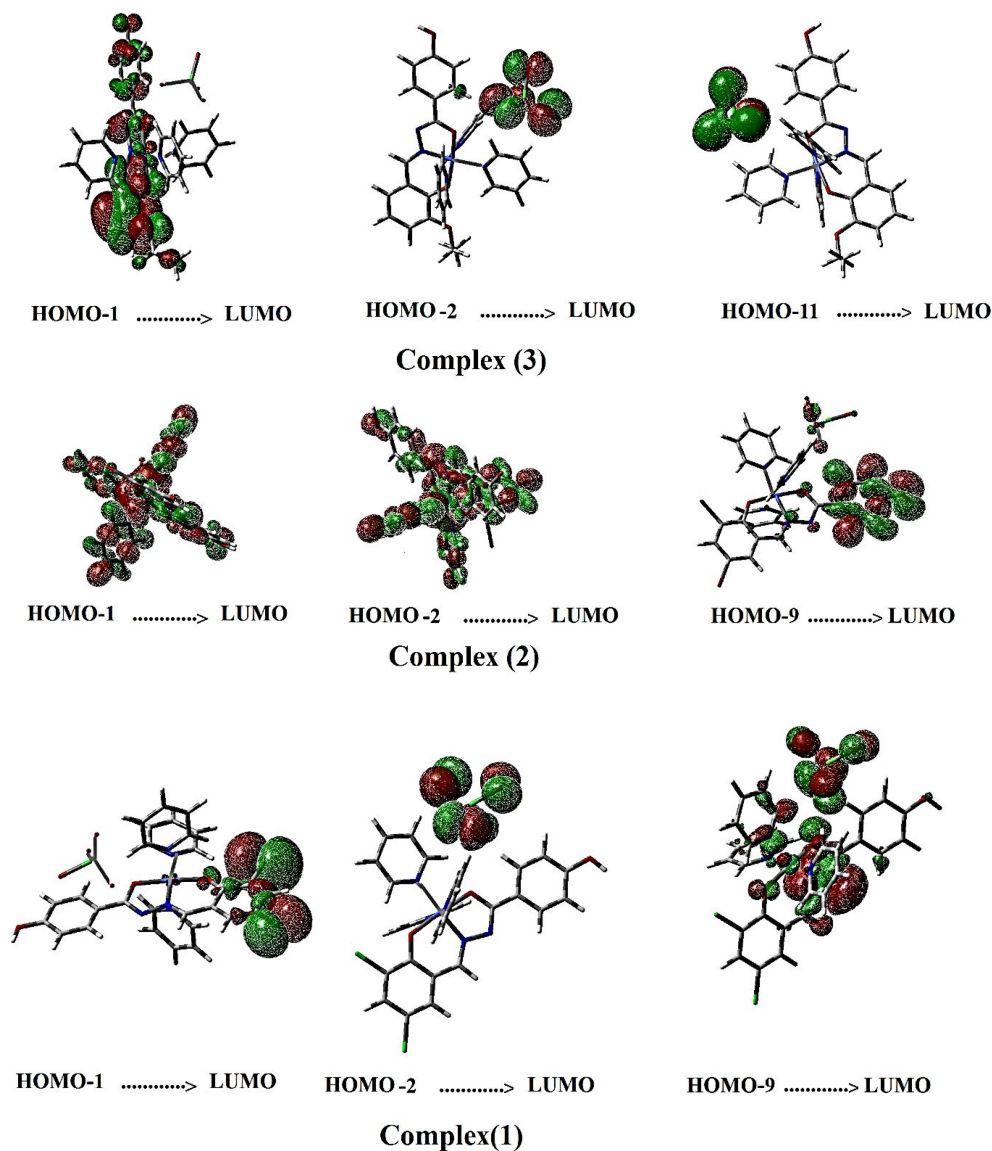
from these parameters, the complex (**2**) with a higher energy gap, HOMO and LUMO, is a more stable structure than the other complexes and is known as a harder molecule. This result may be due to the presence of stronger interactions and hydrogen bonds in the complex (**2**) structure than in the other complexes. Furthermore, the negative energy levels of LUMO and HOMO show that all three complexes were stable.[70] The molecular orbitals of the Co(III) complexes are presented in Figure 7. The calculated HOMO-1 → LUMO (97.00% occupied volume of orbital) energy gap was 1.965 eV, HOMO-2 → LUMO (93.00% occupied volume of orbital) energy gap was 2.308 eV, and HOMO-9 → LUMO (78.00% occupied volume of orbital) energy gap was 2.203 eV of complex (**1**), whereas HOMO-1 → LUMO (97.00% occupied volume of orbital) energy gap was 1.995 eV, HOMO-2 → LUMO (91% occupied volume of orbital) energy gap was 2.313 eV, and HOMO-

9 → LUMO (86% occupied volume of orbital) energy gap was 2.203 eV of complex (**2**), as well as HOMO-1 → LUMO (98%) energy gap was 1.521 eV, HOMO-2 → LUMO (96%) energy gap was 2.136 eV, and HOMO-11 → LUMO (36%) and HOMO-12 → LUMO (54%) energy gap was 2.262 eV of complex (**3**). Table 5 summarizes the main contribution and energy results of the Co(III) complexes (**1–3**) as well as the computed excitation wavelength ($\lambda_{\text{cal nm}}^{-1}$).

3.6.4 | NBO analysis

The NBO analysis was used to further study the hydrogen bonds in the Co(III) complex (**1–3**), the natural charge of the atoms involved in the hydrogen bonds C—H ... O, C—H ... N, and C—H ... C, and other interactions. The results are presented in Table 6. As can be seen from the

TABLE 5 Calculated excitation wavelengths ($\lambda_{cal\ nm}^{-1}$), major contribution, and energy of the studied complexes

Transitions	λ_{cal}	Major contribution	Orbital distribution	Energy
Complex (1)				
HOMO-1 → LUMO	630	97%	On (phenyl ring)$_{aldehyde}$ and center metal	1.965
HOMO-2 → LUMO	437	93%	On the ClO^-_4	2.308
HOMO-9 → LUMO	462	78%	On the pyridine ring, ClO^-_4, and center metal	2.203
Complex (2)				
HOMO-1 → LUMO	620	97%	On all atoms	1.995
HOMO-2 → LUMO	440	91%	On all atoms	2.313
HOMO-9 → LUMO	462	86%	On the (phenyl ring)$_{benzohydrazide}$, and a very small amount is spread on ClO^-_4, center metal	2.203
Complex (3)				
HOMO-1 → LUMO	714	98%	On the ligand and center metal	1.521
HOMO-2 → LUMO	480	96%	On the ClO^-_4	2.136
HOMO-11 → LUMO	448	36%	On the ClO^-_4	2.262
HOMO-12 → LUMO	448	54%	On the ClO^-_4 and a very small amount is spread on (C—H)$_{benzohydrazide}$	2.262

Abbreviations: HOMO, highest occupied molecular orbital; LUMO, lowest unoccupied molecular orbital.

results in Table 6, the low positive charge on the hydrogen atom and the high negative charge on the oxygen atom cause hydrogen bonds in the studied complexes, which are properly formed by the NBO. Another argument is that the large charge difference between the atoms involved in hydrogen bond creation specifies a stronger interaction, and the minor difference designates a weak bond. The maximum charge difference belongs to the contacts O … H, which causes the formation of a hydrogen bond C—H … O, followed by contacts H … N and C … H, which form the interaction C—H … N and C—H … π. These results have also been observed using HS analysis for complex (**1**).

3.7 | Molecular electrostatic potentials

The 3D MEP maps for Co(III) complexes (**1–3**) are presented in Figure 8. The electrostatic potential values of the positive and negative locations in the studied complexes are shown in the color scheme, from red to blue. All three MEP maps in Figure 8 display that O atoms with red have a negative electrostatic potential and they are considered a strong repulsive site for electrophilic attack. Among the oxygen species in the structures, perchlorate oxygen plays the most important role, which causes the formation of a strong hydrogen bond C—H … O. The most likely blue areas are concentrated near the (C—H)$_{pyridine}$ ring, (C—H)$_{aldehyde}$, (H)$_{4-hydroxybenzohydrazide}$, nitrogen, and the central metal for all three complexes, as well as the (C—H)$_{3-ethoxy}$ group for complex (**3**), which

creates a more reactive location for a nucleophilic attack. Also, these sites are accessible for hydrogen bonding because of the presence of highly electronegative atoms, N, O, and C atoms. Using HS analysis, we can show that these results are true. Complex **1** is an excellent example of this.

3.8 | QTAIM theory

The "atom in a molecule" theory is a simple and practical theory that uses electron density analysis to connect the fundamental concepts of chemistry and quantum mechanics. The electron density, according to this theory, is measurable and can determine the shape and appearance. This theory determines which atoms are connected by bonds and which are separated by them. The spatial properties of electron density are considered in this method, which is summarized in critical points. The atoms in the molecule field gradient disappear and are zero at these points, indicating places with the highest electron density. The critical point bonds are one of the most important critical points.

The Laplacian concept of electric charge density, on the other hand, is utilized to determine the places where the electron density is concentrated or absent. We have an electron discharge if the Laplacian electric charge density is positive and the electric charge density at that location is below average (non-covalent bonds such as ionic, hydrogen, or van der Waals bonds), and an electron-rich site if it is negative (covalent and polar bonds). A negative

TABLE 6 The natural charge due to natural bond orbital (NBO) analysis was calculated at level B3LYP/6-311G.

| Compound/ graph set	Q_i
Complex (1)	
Co	1.40
$O_{(aldehyde)}$	−0.651
$O_{(benzohydrazide)}$	−0.706, −0.604
$O_{(ClO4)}$	−0.508, −0.502, −0.462, −0.448
$N_{(HC=N)}$	−0.467
$N_{(N-N)}$	−0.251
$N_{(Py)}$	−0.666, −0.636, −0.636
$C_{(C-H)}$	−0.420, −0.236, −0.229, −0.219, −0.210, −0.064, −0.029
$H_{(C-H)}$	0.297, 0.196, 0.189, 0.177, 0.173, 0.154, 0.117, 0.109
Complex (2)	
Co	1.40
$O_{(aldehyde)}$	−0.710
$O_{(benzohydrazide)}$	−0.605, −0.653
$O_{(ClO4)}$	−0.509, −0.501, −0.463, −0.448
$N_{(HC=N)}$	−0.468
$N_{(N-N)}$	−0.259
$N_{(Py)}$	−0.666, −0.636, −0.630
$C_{(C-H)}$	−0.426, −0.233, −0.229, −0.214, −0.210, −0.137, −0.055, −0.030
$H_{(C-H)}$	0.371, 0.296, 0.230, 0.211, 0.195, 0.189, 0.173, 0.154
Complex (3)	
Co	1.40
$O_{(aldehyde)}$	−0.709
$O_{(benzohydrazide)}$	−0.607, −0.659
$O_{(ClO4)}$	−0.504, −0.503, −0.464, −0.450
$N_{(HC=N)}$	−0.470
$N_{(N-N)}$	−0.252
$N_{(Py)}$	−0.663, −0.631, −0.626
$C_{(C-H)}$	−0.431, −0.283, −0.217, −0.210, −0.180, −0.135, −0.103
$H_{(C-H)}$	0.369, 0.298, 0.230, 0.180, 0.171, 0.151, 0.150, 0.113

charge is defined as an electron-rich place with a Laplacian negative charge density and an electron discharge with a Laplacian positive charge. According to studies, the type of hydrogen bond is determined by the amount of electron density being related to the critical points bond in the range of 0.035 to 0.002 and the Laplacian density of the electric charge being in the range of 0.0139 to 0.002. In an atom in molecule theory, other characteristics are also employed to determine interactions. At the critical point, these parameters include kinetic energy density $G(r)$, potential energy density $V(r)$, and total energy density $H(r)$, and these parameters can also be used to identify interactions. Existing interactions are denoted by an open shell and a closed shell, respectively, to describe the type of bond and its relationships.[55,56,71,72] The open-shell interactions $(((|(V(r))|/(G(r))) > 2)$ and $H(r) < 0)$ are identified, as well as $(((|(V(r))|/(G(r))) < 1)$ and $H(r) > 0)$ closed-shell interactions. Table 7 summarizes the results of the analysis of atom theory in molecules including the electron density parameter $\rho(r)$, Laplacian ($\nabla^2\rho(r)$), kinetic energy density ($G(r)$), potential energy density ($V(r)$), and total electron energy density ($H(r)$), as well as the total energy density of the electron ($H(r)$). The distribution of critical point bonds studied in complexes (**1–3**) as red spheres is shown in Figure 9 of critical point bonds. According to the results obtained from Table 7 and the critical points bond, it can be understood that the discharge of electrons occurs near the surface of the interacting atoms, which is due to the high values of electron density $\rho(r)$ at the bond critical points (BCPs). Metal–ligand bonding (Co—O and Co—N) and Laplace positive sign, and the nature of bonding (Co—N and Co—O) are also recommended in these non-covalent or non-polar interaction complexes. According to the energy parameter analysis, the total energy density of the electron ($H(r)$) that has negative values in BCP is obtained, which is about −0.0066 to −0.240 a.u. for complex (**1**), −0.0065 to −0.243 a.u. for complex (**2**), and −0.0088 to −0.249 a.u. for complex (**3**). This was how to bond (open shell) polar interactions were perceived. The ratio of the potential energy density ($V(r)$) to the kinetic energy density ($G(r)$) is greater than 1 ($G(r)$) is larger than 1 $(((|(V(r))|/(G(r))) > 1)$; the strength of this confirms interactions and shows a kind of intermediate interaction. In general, metal–ligand bonds (Co—O and Co—N) are predicted to be the structures of the studied non-covalent complexes (**1–3**), with a significant contribution of ionic nature.[55]

3.9 | Molecular docking studies

Coronaviruses have positive, single-stranded RNA with enveloped structures. These viruses are composed of structural and non-structural proteins. Structural protein Spike glycoprotein (S) plays an important role. For the SARS-CoV virus to enter the host cell, the glycoprotein must be able to bind to both the host receptor and the ACE-2.[73,74] Unstructured proteins play an important role in virus replication and include papain-like protease

FIGURE 8 Molecular electrostatic potential (MEP) maps were calculated at the B3LYP/6311-G level for the studied complexes.

Complex (1)

Complex (2)

Complex (3)
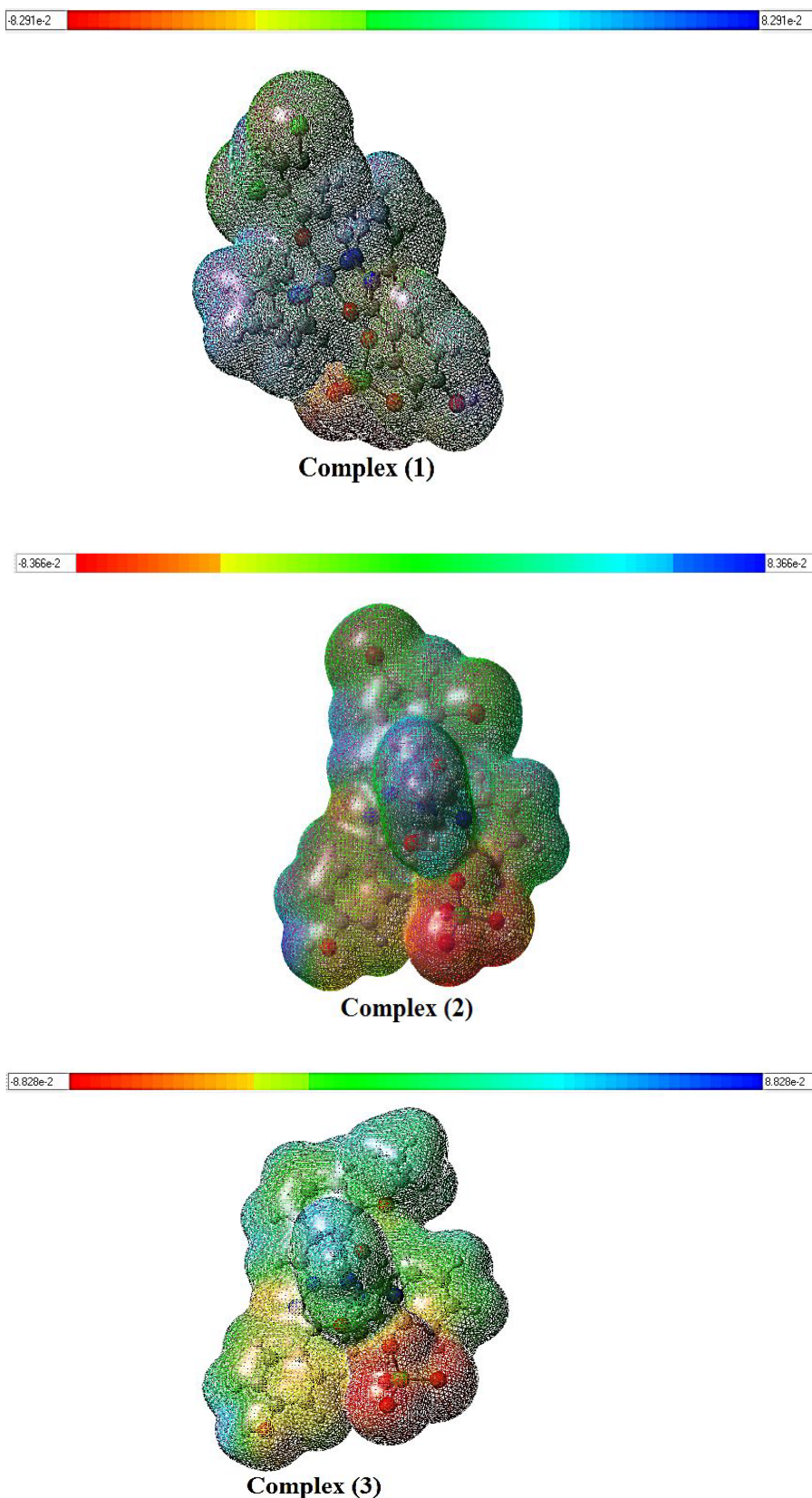
(PL pro) and 3-chymotrypsin protease (3CL pro or M pro). Also, the main SARS-CoV-2 protease consists of three domains. At the interface of domain I and domain II is the active site of the protein, which has a Cys–His pair. In addition, it binds a domain II linker to domain III to perform a critical function for protein dimerization.

TABLE 7 Topological properties $\rho(r)$ and $\nabla^2\rho(r)$ (a.u.), kinetic energy density ($G(r)$, in a.u.), potential energy density ($V(r)$, in a.u.), and total energy density ($H(r)$, in a.u.) for bond critical point (BCP) of the studied metal–ligand interactions at the B3LYP/SDD(6-311G) level for the studied complexes

Intramolecular interaction	$\rho(r)_{BCP}$	$\nabla^2\rho(r)_{BCP}$	$G(r)_{BCP}$	$V(r)_{BCP}$	$H(r)_{BCP}$	$(|(V(r))|/(G(r)))_{BCP}$
Complex (1)						
(Co—N)$_{Py}$	0.0824	0.1016	0.1116	−0.1216	−0.0100	1.089
	0.0903	0.1049	0.1189	−0.1329	−0.0139	1.117
	0.0911	0.1048	0.1197	−0.1346	−0.0149	1.124
(Co—O)$_{aldehyde}$	0.0903	0.1386	0.1452	−0.1518	−0.0066	1.045
(Co—O)$_{4\text{-hydroxy benzohydrazide}}$	0.0982	0.1352	0.1471	−0.1590	−0.0119	1.080
(Co—N)$_{C=N}$	0.1079	0.1247	0.1487	−0.1727	−0.0240	1.161
Complex (2)						
(Co—N)$_{Py}$	0.0823	0.1016	0.1116	−0.1216	−0.0099	1.089
	0.0902	0.1050	0.1190	−0.1329	−0.0139	1.116
	0.0909	0.1049	0.1196	−0.1344	−0.0147	1.123
(Co—O)$_{aldehyde}$	0.0901	0.1377	0.1443	−0.1509	−0.0065	1.045
(Co—O)$_{4\text{-hydroxy benzohydrazide}}$	0.0981	0.1350	0.1469	−0.1588	−0.0118	1.081
(Co—N)$_{C=N}$	0.1084	0.1248	0.1492	−0.1735	−0.0243	1.162
Complex (3)						
(Co—N)$_{Py}$	0.0819	0.1021	0.1118	−0.1215	−0.0096	1.086
	0.0896	0.1054	0.1189	−0.1324	−0.0134	1.113
	0.0898	0.1049	0.1191	−0.1333	−0.0141	1.119
(Co—O)$_{aldehyde}$	0.0946	0.1418	0.1506	−0.1594	−0.0088	1.058
(Co—O)$_{4\text{-hydroxy benzohydrazide}}$	0.0965	0.1338	0.1450	−0.1562	−0.0112	1.077
(Co—N)$_{C=N}$	0.1092	0.1247	0.1497	−0.1746	−0.0249	1.166

It should also be noted that the action of a viral spike protein is one of the most important pathophysiological mechanisms that causes the virus to enter the host with the help of the ACE-2 receptor. In addition, hepcidin regulates iron metabolism with ferroportin for iron to enter cells. Iron metabolism is of particular importance in the delivery of several organs. In SARS-CoV-2 infection, it leads to ferroptosis, which disrupts iron metabolism.[75] One of the causes of hypoxia lung disease is anemia. Effective protocols are present to prevent Covid-19 including a drug that disrupts the virus life cycle by blocking ACE-2 receptors or inhibiting SARS-CoV-2.[76] The second way is using an iron chelating agent to combine with excess iron due to impaired metabolism. The third method is anti-inflammatory drugs like phosphodiesterase-4 inhibitors for the treatment of pneumonia.[77,78] In this study, Co(III) complexes from hydrazide derivatives were synthesized and studied against the main protease enzyme SARS-CoV-2 (M pro) and the human ACE-2 receptor via molecular simulation. One of the coronavirus targets is the main protease (M pro),[79,80] ACE-2 is one of the important therapeutic targets,[81,82] and antiviral drugs against SARS-CoV-2, which plays an important role for SARS-CoV acts in entering target cells. Figures 10b,d, 11b,d, and 12b,d indicate the different interactions of the Co(III) complexes (1–3) with selected biological targets of the 6Y2F and 6M0J protein. The results of molecular docking showed that all three complexes could interact effectively with the molecular targets of SARS-CoV-2 and ACE-2 and penetrate the active site of the protein. The total energies of the system Co(III) complexes (1–3) were estimated at −65.69, −82.08, and −56.67 kcal mol^{-1}, respectively, using 6Y2F protein targets. Furthermore, the total energy of the system complexes (1–3) was calculated to be −117.49, −148.80, and −136.92 kcal mol^{-1}, respectively, using 6M0J protein targets. Co(III) complexes (2) performed better than complexes (1) and (3), with the lowest total energy of the system (−82.08 and −148.80 kcal mol^{-1}, respectively), and more amino acids were able to penetrate into the active cavity, and the system's total energy was calculated negatively. In general, the biological study using the molecular docking method showed good potential in inhibiting human ACE-2 target

FIGURE 9 Molecular graphs and distribution of bond critical points (BCPs) for Co(III) complexes (**1–3**). BCPs and bond paths connecting BCP are represented as red spheres and black, respectively. The BCPs at the bond paths connecting atoms around center metal (M ... O and M ... N in Table 7) are highlighted by yellow arrows, in the figure.
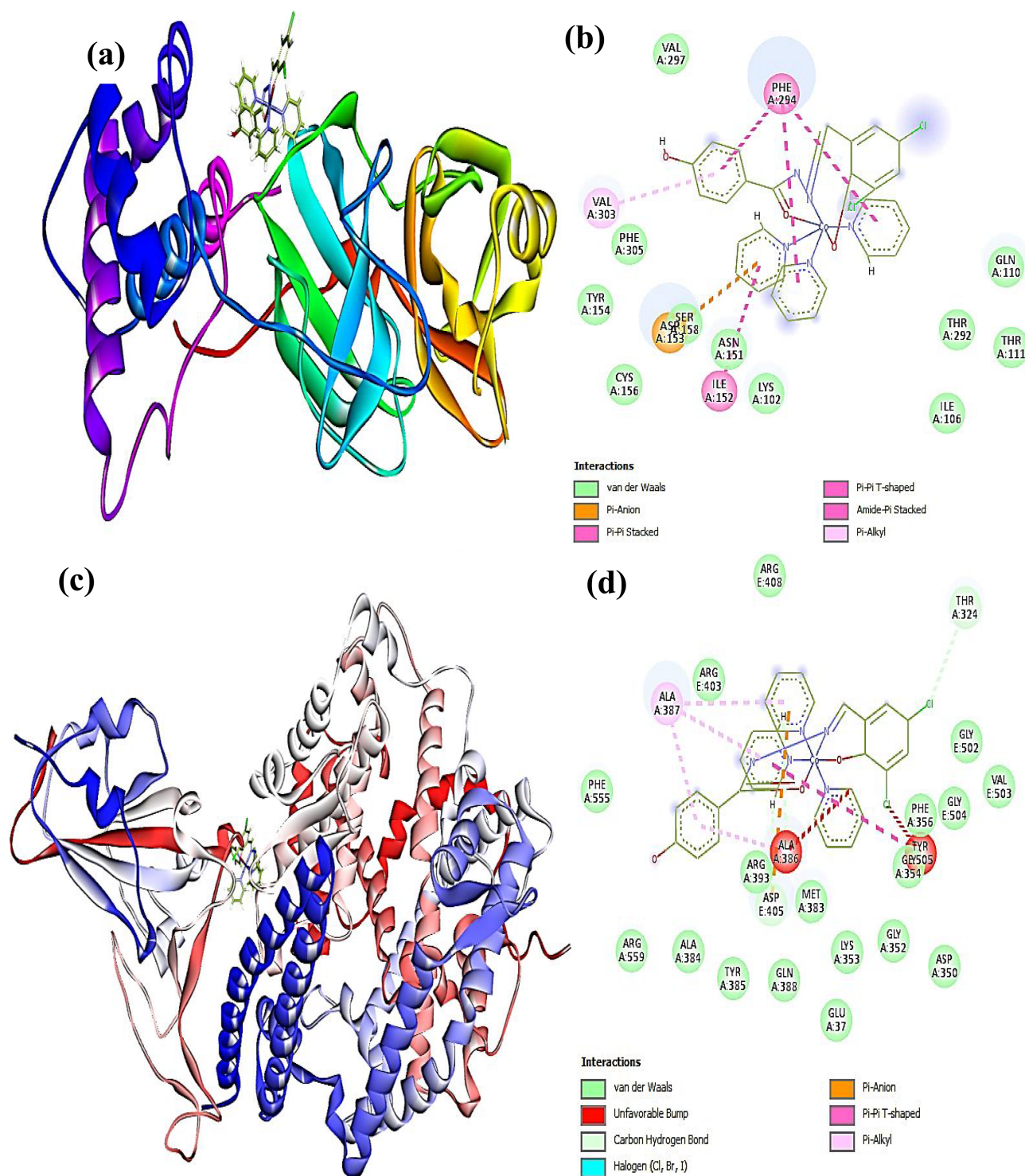
Complex (1)
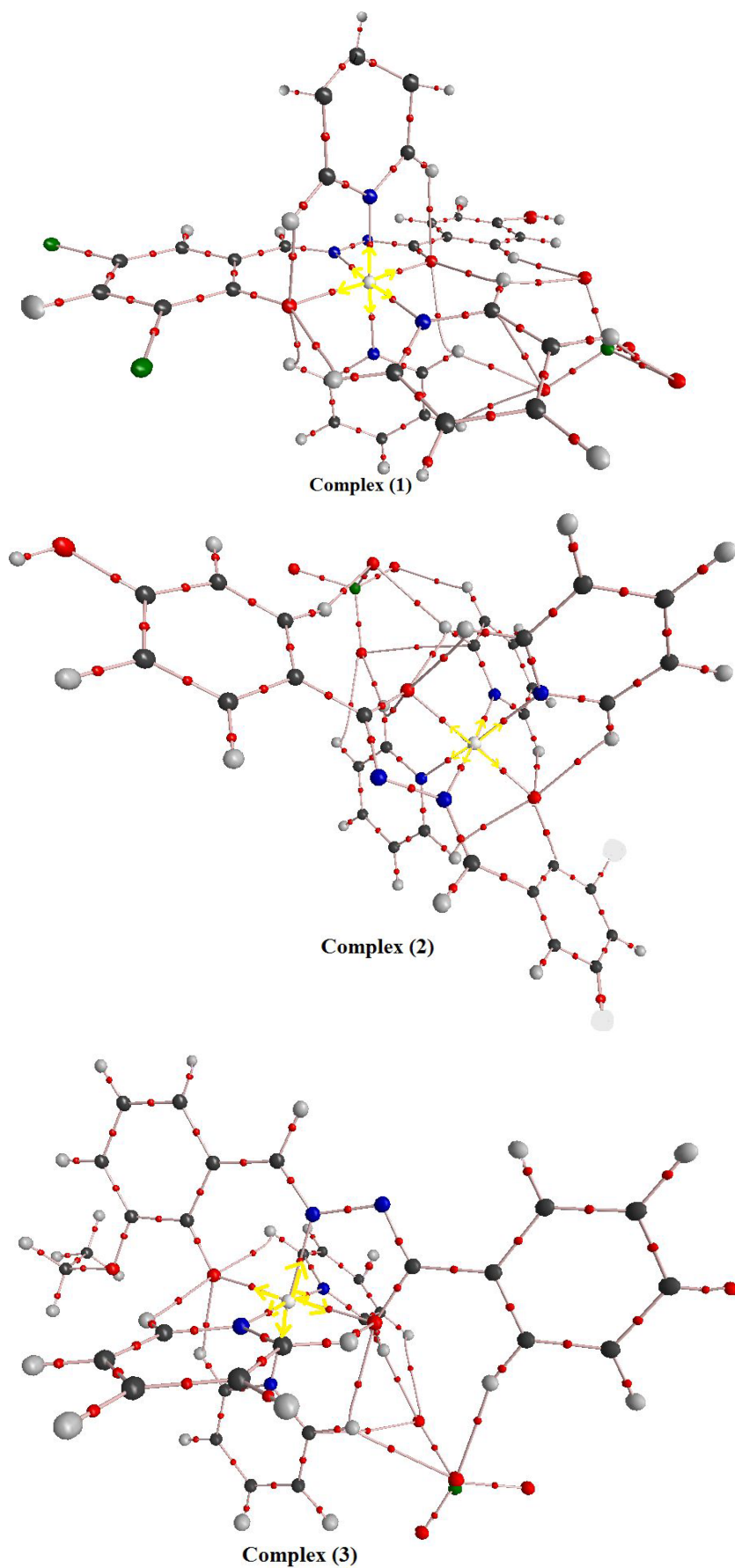
Complex (2)

Complex (3)

FIGURE 10 (a, c) Docking model of the complex (**1**) and (b, d) the binding method of the corresponding respective receptor inhibitor of the important amino acids involved (two- and three-dimensional interactions) of (b) ID: 6Y2F and (d) ID: 6M0J) complex (**1**) are shown.

protein (6M0J) for complexes relative to the SARS-CoV-2 protein (6Y2F). As can be realized from the results, all three studied complexes correlate well with the active sites of the amino acid proteins 6Y2F and 6M0J, and by creating various interactions such as van der Waals, carbon hydrogen bonding, conventional hydrogen bonding,

and π-type interactions can be recommended as suitable inhibitors to cause disorder. The function of the 6Y2F and 6M0J proteins is that they disrupt the function of virus proteins, which are in fact the keys that the coronavirus uses to enter host cells. It has been proposed that these complexes can inhibit SARS-CoV-2 by interfering
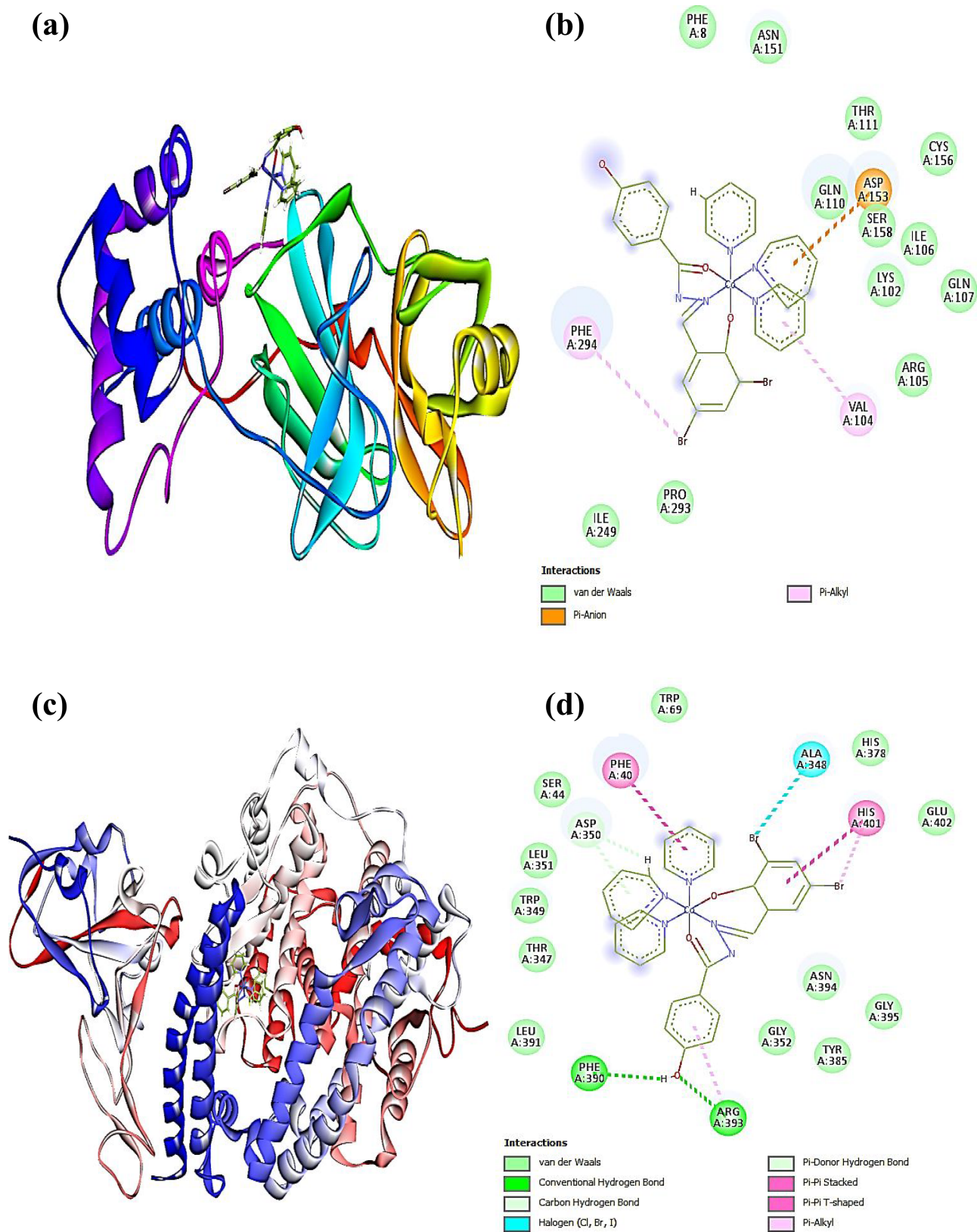
(a)

(b)

(c)

(d)

FIGURE 11 (a, c) Docking model of the complex (**2**) and (b, d) the binding method of the corresponding respective receptor inhibitor of the important amino acids involved (two- and three-dimensional interactions) of (b) ID: 6Y2F and (d) ID: 6M0J) complex (**2**) are shown.

(a)

(b)

Interactions

van der Waals	Pi-Cation
Unfavorable Bump	Pi-Anion
Conventional Hydrogen Bond	Pi-Pi T-shaped
Carbon Hydrogen Bond	Pi-Alkyl

(c)

(d)

Interactions

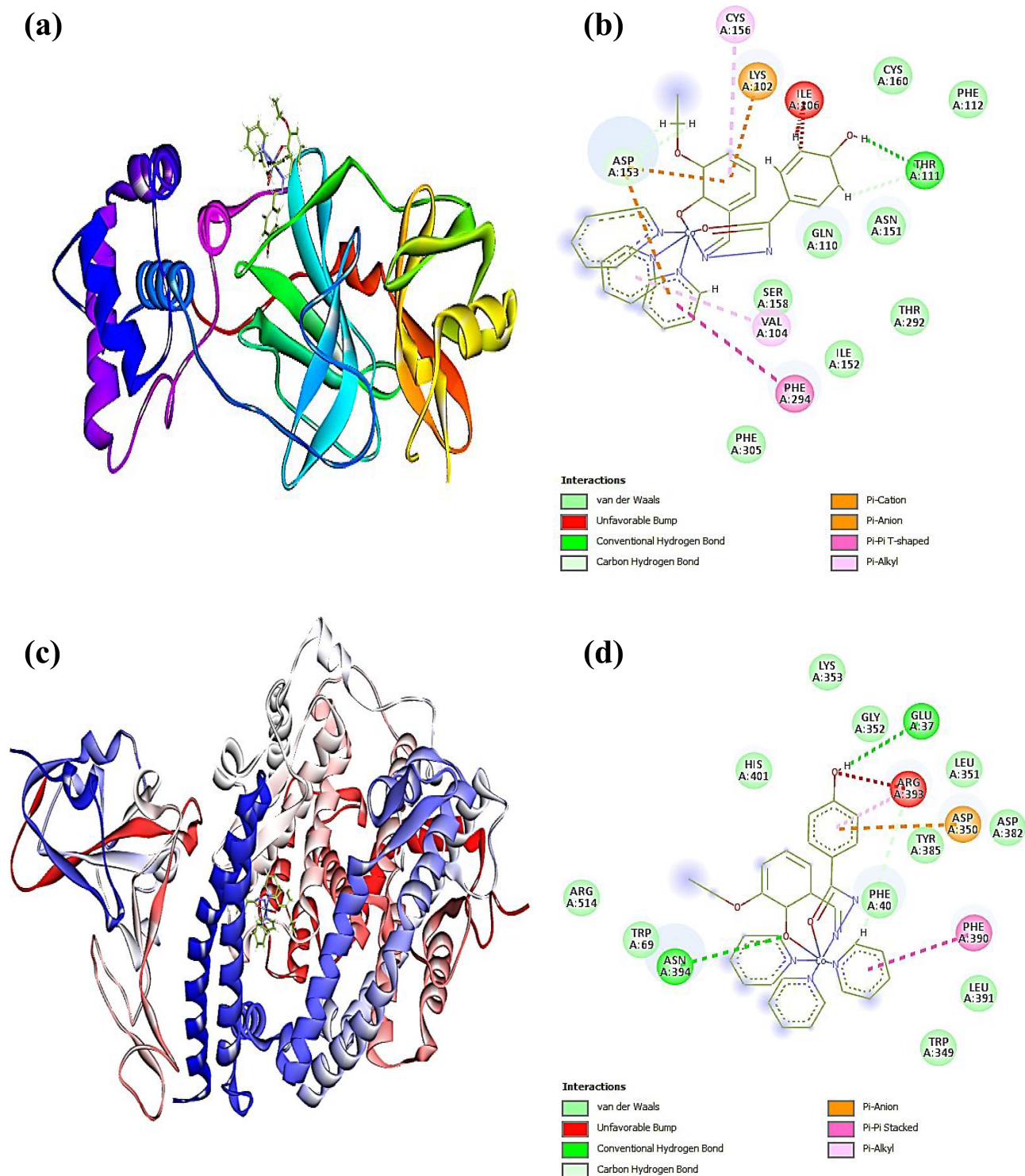|	
van der Waals	Pi-Anion
Unfavorable Bump	Pi-Pi Stacked
Conventional Hydrogen Bond	Pi-Alkyl
Carbon Hydrogen Bond	

FIGURE 12 (a, c) Docking model of the complex (**3**) and (b, d) the binding method of the corresponding respective receptor inhibitor of the important amino acids involved (two- and three-dimensional interactions) of (b) ID: 6Y2F and (d) ID: 6M0J) complex (**3**) are shown.

with the function of virus proteins. For the best understanding of how the complexes bind, the dominant interactions for the best inhibitors of each receptor are summarized as non-covalent interactions with the surrounding amino acids in Table 8, Figures 10–12, as well as in the following sections: (b, d). The complex (**2**) with the highest inhibitory activity against the SARS-CoV-2 protein (6Y2F) and human ACE-2 target protein (6M0J) interacted with the following active amino acid residues: ILE 106, ILE 249, VAL 104, ARG 105, GLN 107, GLN

TABLE 8 Amino acid interaction of the active site of the receptor with the strongest inhibitor

Complexes	Total energy of the system (kcal mol^{-1})	Surrounding amino acids
Combined receptor: SARS-CoV-2 protein (ID: 6Y2F)		
(**1**)	−65.69	LYS A: 102, ILE A: 106, GLN A: 110, THR A: 111, ASN A: 151, ILE A: 152, ASP A: 153, TYR A: 154, CYS A: 156, SER A: 158, THR A: 292, PHE A: 294, VAL A: 297, VAL A: 303, PHE A: 305.
(**2**)	−82.08	PHE A: 8, LYS A: 102, VAL A: 104, ARG A: 105, ILE A: 106, GLN A: 107, GLN A: 110 THR A: 111, ASN A: 151, ASP A: 153, CYS A: 156, SER A: 158, ILE A: 249, PRO A: 293, PHE A: 294.
(**3**)	−56.67	VAL A: 104, ILE A: 106, GLN A: 110, THR A: 111, PHE A: 112, ASN A: 151, ILE A: 152, ASP A: 153, CYS A: 156, SER A: 158, CYS A: 160, THR A: 292, PHE A: 294, PHE A: 305.
Combined receptor: human ACE-2 target protein (ID: 6M0J)		
(**1**)	−117.49	GLU A: 37, THR A: 324, ASP A: 350, GLY A: 352, LYS A: 353, GLY A: 354, PHE A: 356, MET A: 383, ALA A: 384, TYR A: 385, ALA A: 386, ALA A: 387, GLN A: 388, ARG A: 393, ARG A: 403, ASP A: 405, ARG A: 408, GLY A: 502, VAL A: 503, GLY A: 504, TYR A: 505, PHE A: 555 ARG A: 559.
(**2**)	−148.80	PHE A: 40, SER A: 44, TRP A: 69, THR A: 347, ALA A: 348, TRP A: 349, ASP A: 350, LEU A: 351, GLU A: 352, HIS A: 378, TYR A: 385, PHE A: 390, LEU A: 391, ARG A: 393, ASN A: 394, GLU A: 395, HIS A: 401, GLU A: 402.
(**3**)	−136.92	GLU A: 37, PHE A: 40, TRP A: 69, TRP A: 349, ASP A: 350, LEU A: 351, GLU A: 352, LYS A: 353, ASP A: 382, THR A: 385, PHE A: 390, LEU A: 391, ARG A: 393, ASN A: 394, HIS A: 401, ARG A: 514.

FIGURE 13 (a–c) Hirshfeld surfaces corresponding produced from an atomic spherically averaged electron density. The color code on the Hirshfeld surfaces displays the geometrical function d_{norm} in three directions for complex (**1**).
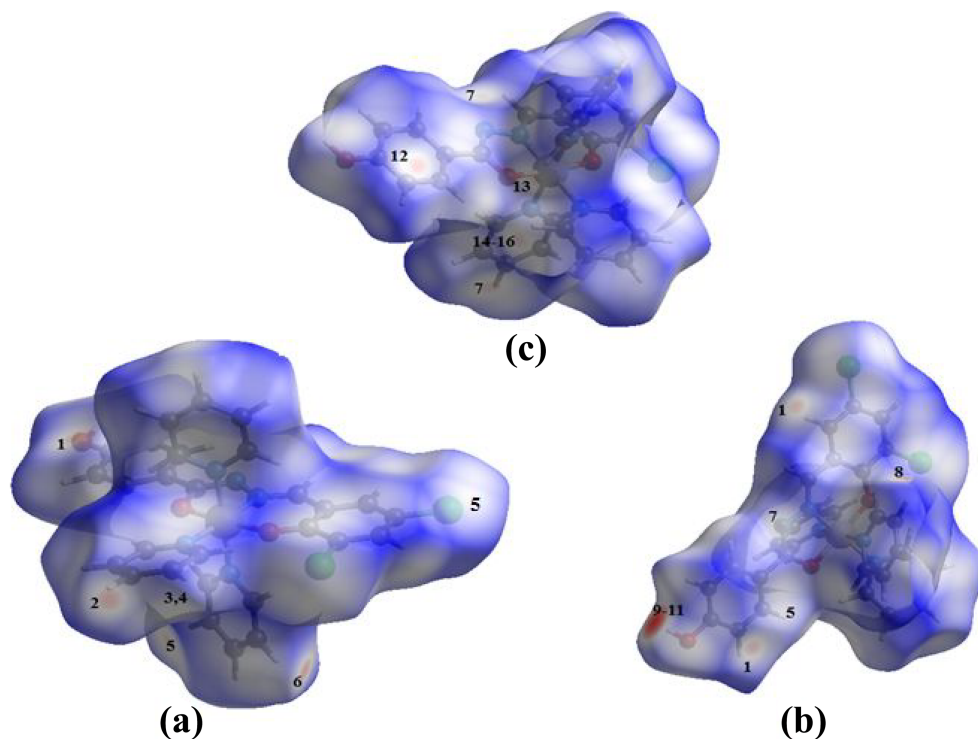
110, LYS 102, THR 111, ASN 151, ASP 153, CYS 156, PRO 293, PHE 294, GLU 352, LEU391, TRP 69, ALA 348, ARG 393, and so forth through non-covalent interaction (Figure 11b,d). Complex (**2**) was surrounded by aspartic acid (ASP A: 153 [for 6Y2F]) and formed a Pi–anion interaction between the amino acid and the pyridine ring. Pi–alkyl interactions were discovered between the Br atom of the ligand part and amino acids with

TABLE 9 Hydrogen bond and short contacts to be prominent in complex (**1**)

D—H ... A	$\delta(D$—H) (Å)	d(H ... A) (Å)	d(D ... A) (Å)	$\angle$ (DHA) (°)	Label	Color code
H5A—H5A ... C13A	0.950	2.749	3.592	148.39	(**1**)	Light red spot
C4B—H4B ... O4E	0.950	2.517	3.318	142.15	(**2**)	Light red spot
C5B—H5B ... O1E	0.950	2.607	3.191	120.03	(**3**)	Light red spot
C5B ... O1E	-	-	3.191	-	(**4**)	Light red spot
Cl5D ... C3D	-	-	3.306	-	(**5**)	Light red spot
C5D—H5D ... O2E	0.950	2.502	3.370	151.95	(**6**)	Light red spot
C4D—H4D ... N9A	0.950	2.693	3.588	157.41	(**7**)	Light red spot
C3C—H3C ... O1E	0.950	2.477	3.312	146.66	(**8**)	Dark red spot
C13A—H13A ... O3E	0.950	1.975	2.749	145.68	(**9**)	Dark red spot
C15A—H15 ... O3E	0.950	2.648	3.347	130.90	(**10**)	Dark red spot
O14A ... O3E	-	-	2.814	-	(**11**)	Dark red spot
C5A ... C14A	-	-	3.400	-	(**12**)	Dark red spot
C6C—H6C ... O4E	0.950	2.595	3.477	154.58	(**13**)	Dark red spot
C2B ... O3E	-	-	3.191	-	(**14**)	Light red spot
C2B—H2B ... O3E	0.950	2.528	3.191	127.0	(**15**)	Light red spot
C3B—H3B ... O3E	0.950	2.662	3.246	120.28	(**16**)	Light red spot

hydrophobic and aliphatic side chains, such as phenyl alanine (PHE A: 294 [for 6Y2F]), as well as histidine (HIS A: 401 [for 6M0J]). Interactions were also observed between the amino acids including valine (VAL A: 104 [for 6Y2F]) and arginine (ARG A: 393 [for 6M0J]). In addition, the interaction of halogen with alanine (ALA A: 348) and the Br atom (for 6M0J). The polar segments interact with complex (**2**) with arginine (ARG A: 393) and phenyl alanine (PHE A: 40, 390) amino acid residues (for 6M0J). The orientation of the cobalt complexes is almost similar so that the planar arrangement of the salicylic aldehyde rings allows the complexes to be pulled in the right direction at the active site of the receptors and to interact well with the amino acids. The planar amine rings are oriented toward the appropriate active site and bind to the amino acids on the outer surface of the site. It should be noted that the hydrophobic interactions of Br atoms in these complexes have increased the inhibitory power of these complexes. Schiff base metal complexes can be effectively bonded through hydrophobic interactions. Planar sections coordinated with the central metal can help stabilize the complexes.

3.10 | Investigation of intermolecular interactions by HS analysis and FPs plot of the complex (1)

From the d_{norm} HS analysis of the molecule Co(III) of complex (**1**) in Figure 13a–c, the intense red and bright red regions on the surface labeled (**2**, **3**, **6, 8–10**, **13**, **15**, and **16**) represent H ... O/H ... O hydrogen bonds associated with C—H ... O hydrogen bond interactions between the (C—H)$_{Pyridine and 4-hydroxy benzohydrazide}$ and (O)$_{ClO4}$ units. The regions delineated into the C ... H/H ... C, O ... C, N ... H/H ... N, O ... O, C ... C, and C ... Cl contacts appear as extremely small red areas. The light red spots on the HS near the (C—H)$_{benzaldehyde ring}$ and the (C)$_{4-hydroxy benzohydrazide}$ ring in the region (**1**) reflect C5A—H5A ... C13A interactions. Furthermore, the presence of very light red spots in areas **4**, **5**, and **14** on the HS designates the existence of C5B ... O1E, Cl4A ... C3D, and C2B ... O3E interactions, respectively, between the (C)$_{Pyridine}$ ring and (O)$_{ClO4}$ in regions (**4 and 14**), and the (Cl)$_{benzaldehyde}$ ring and the (C)$_{Pyridine}$ ring in the region (**5**). The bright red spot in the label (**7**) supports the presence of the N9A ... H4D—C4D interaction, which is made by the short contact of the (N)$_{4-hydroxybenzohydrazide}$ group with the (C—H)$_{Pyridine}$ group. The red area on the HS of two neighboring molecules signifies the interactions between oxygen atoms of two groups (O)$_{ClO4}$ and (O)$_{benzaldehyde}$ ring in areas **11** (O14A ... O3E) as well as two groups (C)$_{benzaldehyde}$ ring and (C)$_{4-hydroxybenzohydrazide}$ group in the region **12** (C5A ... C14A). Table 9 provides additional information from HS analysis and short contacts.

The geometric function created by d_i and d_e in the Co(III) complex is shown in Figure 14, where the donor and acceptor areas are shown in green and red, respectively. The acceptor area is highlighted with almost flat

FIGURE 14 The color code on the Hirshfeld surfaces represents the geometrical function created with d_i, d_e, *curvedness*, and *shape index* function of the complex (**1**).

Shape index

curvedness

d_e d_i
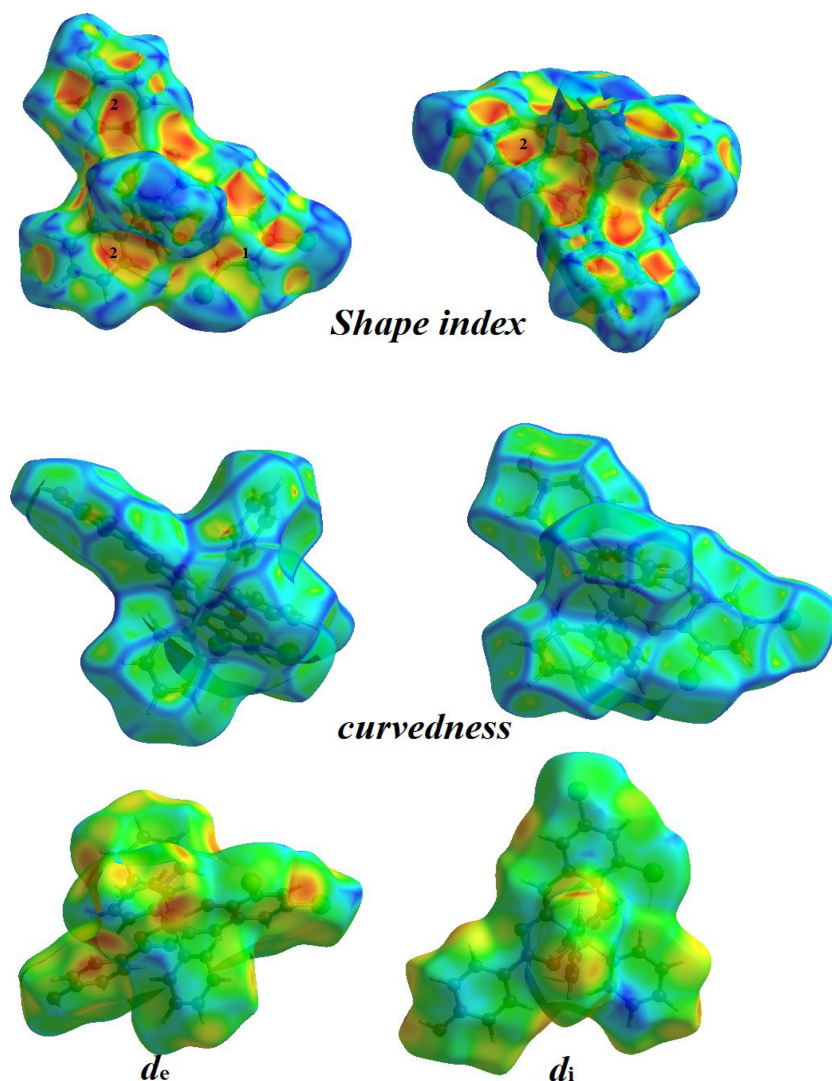
surfaces and red spots, and the donor area is highlighted with flat surfaces and green. Also, the presence of $\pi \cdots \pi$ interactions is confirmed by using light blue color on the surface of Hirshfeld in the form of a six-corner surface with light-blue spokes, which consists of the overlap and proximity of two phenyl rings. In Figure 14, the HS is shown by the mapped *curvedness* function. The planner surface, shown with a blue outline and delineated on the aromatic rings on Hirshfeld's surface, clearly proves the π ... π interactions. Also, the shape index function is used to better show the HSs in Figure 14 and to look at how interactions work. These functions are highlighted by creating blue and red colors on the HS. The number 1 specified in the figure indicates the interactions, π ... π, which through the bow-tie pattern of red and blue triangles indicates a specific accumulation of phenyl rings.[54-56] In addition, patterns of "red π- holes" on the shape index surface with the number 2 on the HS have been specified[54-56] to distinguish the C—H ... π interactions between the benzaldehyde rings and CH groups.

The total fingerprint area, signified as a combination of d_i plot versus d_e plot alongside with the specified main intermolecular exchanges, is also exhibited in Figure 15. H ... H (region **1**) exchanges have the largest occupied (36.3%) of the HS; the sharp areas are concentrated in the form of an almost blue diagonal, about $1.1 < d_e$, $d_i < 2.7$ Å. In region **2**, a pair of wings displays C ... H/H ... C interaction, which causes the C—H ... π exchanges. This interaction covers approximately 19.6% of the surface and creates the contact C ... H/H ... C with (d_i +- $d_e \approx 2.6$ Å). Furthermore, the H ... O/O ... H (region **3**) short contacts (15.9% contribution) are shown as a pair of asymmetric blue spikes in the top and bottom parts of the left side of the diagram with a minimum amount of $d_i + d_e \approx 1.1$–2.8 Å, which confirms the interaction of C—H ... O. The Cl ... C/C ... Cl (region **4**, 9.4% contribution) interactions shown as the blue dots are diagonally centered in the center of the graph, and the H ... Cl/Cl ... H (region **5**, 6.9% contribution) interactions as wing are placed on the upper left and lower right sides of the
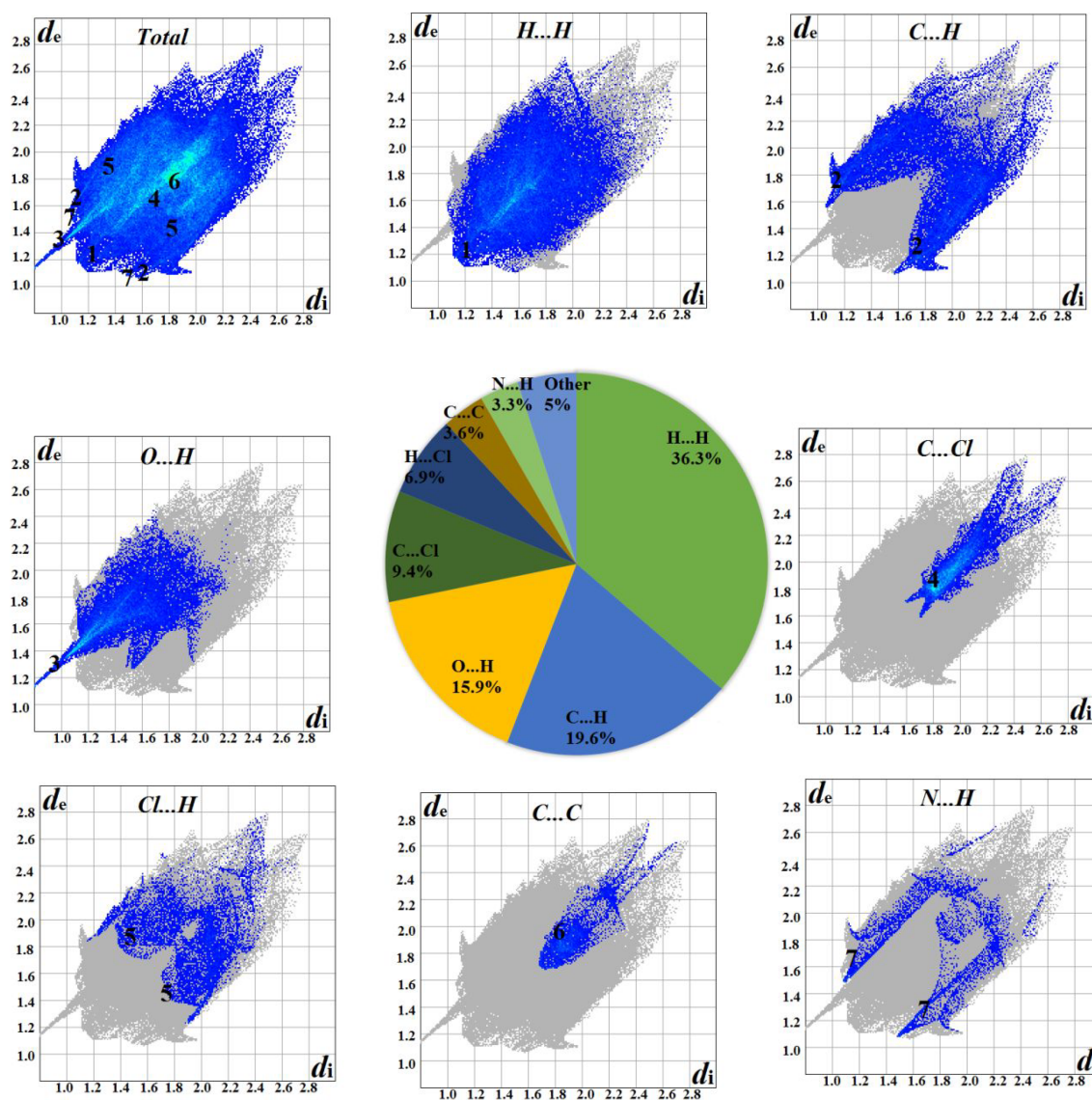
FIGURE 15 Corresponding 2D fingerprint plots generated from an atomic spherically averaged electron density are determined for Co(III) complex (**1**).

Interactions	Percentage of participation	d_i	d_e	$d_i + d_e$
Complex (1)				
H ... H	36.3	1.1–2.6	1.2–2.6	2.2
C ... H	19.6	1.5–2.8	1.5–2.8	2.6
O ... H	15.9	0–2.2	1.1–2.4	1.1–2.8
Cl ... C	9.4	1.7–2.8	1.7–2.8	2.3
Cl ... H	6.9	1.7–2.8	1.7–2.8	3.1
H ... N	3.6	1.7–2.7	1.7–2.8	3.4
C ... C	3.3	1.5–2.6	1.5–2.6	2.6

TABLE 10 The information obtained from the 2D fingerprint graph with a larger contribution interaction for the complex (**1**)

diagram. Also, the C ... C (region **6**, occupying 3.6%) interaction, which signifies the $\pi\cdots\pi$ interaction between the two aldehyde and amine ligand rings, is realized as a

specific image of the blue area, nearly located in the center of the diagram. The H ... N/N ... H exchanges (region **7**) are signified by two spikes in the top left part ($d_e > d_i$

H ... N) and bottom right part ($d_e < d_i$ N ... H) of the plots, comprising 3.3%. These interactions provide the interactions with the fewest $d_i + d_e \approx 2.6$ Å. Other weaker interactions with a contribution of less than 2.0% are involved in the crystal structure of this complex, causing weak intramolecular exchanges, including contacts Cl ... O (1.9%), C ... O (1.9%), N ... N (0.6%), C ... N (0.3%), and Cl ... N (0.3%), which were not examined. Table 10 shows the relative contributions of the fingerprint diagram results, and Figure 15 shows the results of Table 10 as a circular graph.

4 | CONCLUSION

Three new Co(III) complexes were synthesized from hydrazide derivatives and characterized using elemental analysis, FT-IR spectroscopy, UV–Vis spectroscopy, and cyclic voltammetry. The crystal structure of the complex (**1**) was determined using X-ray crystallographic analysis. All three Co(III) complexes were analyzed using DFT, MEP, QTAIM, and HS theoretical studies. Computational results of FT-IR and UV–Vis spectra theoretical studies are consistent with experimental results. Complex (**2**) was calculated with greater stability and greater hardness with a higher HOMO–LUMO energy gap compared with the other complexes. The theory of QTAIM proposes metal–ligand interactions of a non-covalent ionic nature. Theoretical studies were performed with new insights to determine the intermolecular interaction in the crystal structures of complex (**1**). In addition, intermolecular interactions with different percentages were obtained using a two-dimensional fingerprint diagram. Furthermore, molecular simulation studies were performed and all three structures showed good results relative to coronavirus inhibitory activity, but complex (**2**) showed better results than the other complexes and could be used as a potential candidate drug for SARS-CoV-2 protein (PDB ID: 6Y2F) and ACE-2 target human protein (6M0J) recommended.

AUTHOR CONTRIBUTIONS
Mehdi Salehi: Investigation; supervision. **Maciej Kubicki:** Formal analysis; investigation. **Rahime Eshaghi Malekshah:** Software.

DATA AVAILABILITY STATEMENT
The data that support the findings of this study are available in the supporting information of this article.

ORCID
Sakineh Parvarinezhad https://orcid.org/0000-0001-5237-431X
Mehdi Salehi https://orcid.org/0000-0002-1335-1032
Maciej Kubicki https://orcid.org/0000-0001-7202-9169
Rahimeh Eshaghi Malekshah https://orcid.org/0000-0003-1835-2605

REFERENCES
[1] N. Mondal, S. Mitra, V. Gramilich, S. O. Ghodsi, K. M. A. Malik, *Plyhedron* **2001**, *20*, 135.
[2] M. K. Trivedi, A. Branton, D. Trivedi, G. Nayak, K. Bairwa, S. Jana, *Anal. Bioanal.* **2015**, *6*(5), 1000265.
[3] J. Liu, Z. Liu, S. Yuan, J. Liu, *J. Mol. Struct.* **2013**, *1037*, 191.
[4] P. Tyagi, S. Chandra, B. S. Saraswat, D. Yadav, *Mol. Biomol. Spectrosc.* **2015**, *145*, 155.
[5] K. Das, C. Sinha, A. Datta, N. Revaprasadu, *J. Chem. Crystallogr.* **2011**, *41*, 1032.
[6] O. Pouralimardan, A. C. Chamayou, C. Janiak, H. H. Monfared, *Inorg. Chim. Acta* **2007**, *360*, 1599.
[7] R. Bikas, M. Ghorbanloo, R. Sasani, I. Pantenburg, G. Meyer, *J. Coord. Chem.* **2017**, *70*, 819.
[8] B. I. N. Mladenova, G. T. Momekov, *Bulg. Chem. Commun.* **2017**, *49*, 83.
[9] N. Noshiranzadeh, A. Heidari, F. Haghi, R. Bikas, T. Lis, *J. Mol. Struct.* **2017**, *1128*, 391.
[10] P. Dandawate, K. Vemuri, E. M. Khan, M. Sritharan, S. Padhye, *Carbohydr. Polym.* **2014**, *108*, 135.
[11] L. G. S. Souza, M. C. S. Almeida, T. L. G. Lemos, P. R. V. Ribeiro, E. S. Brito, V. L. M. Silva, A. M. S. Silva, R. B. Filho, J. G. M. Costa, F. F. G. Rodrigues, F. S. Barreto, M. O. Moraes, *Bioorg. Med. Chem. Lett.* **2016**, *26*, 435.
[12] Y. Wang, H. Yan, C. Ma, D. Lu, *Bioorg. Med. Chem. Lett.* **2015**, *25*, 4461.
[13] R. Eshkourfu, B. Cobeljic, M. Vujcic, I. Turel, A. Pevec, K. Sepcic, M. Zec, S. Radulovic, T. S. Radic, D. Mitic, K. Andjelkovic, D. Sladic, *J. Inorg. Biochem.* **2011**, *105*, 1196.
[14] A. A. Caro, A. Commissariat, C. Dunn, H. Kim, S. L. Garcia, A. Smith, H. Strang, J. Stuppy, L. P. Desrochers, T. E. Goodwin, *Biochim. Biophys. Acta* **1850**, *2015*, 2256.
[15] K. Vasantha, G. Basavarajaswamy, M. V. Rai, P. Boja, V. R. Pai, N. Shruthi, M. Bhat, *Bioorg. Med. Chem. Lett.* **2015**, *25*, 1420.
[16] G. L. Backes, D. M. Neumann, B. S. Jursic, *Bioorg. Med. Chem.* **2014**, *22*, 4629.
[17] Y. Burgos-Lopez, J. Del Pla, L. M. Balsa, I. E. Leon, G. A. Echeverria, O. E. Piro, J. Garcia-Tojal, R. Pis-Diez, A. C. Gonzalez-Baro, B. S. Parajon-Costa, *Inorg. Chim. Acta* **2019**, *487*, 31.
[18] D. Li, S. Wang, H. Xu, Y. Yang, S. Zeng, J. Zhao, D. Wang, J. Dou, *Inorg. Chim. Acta* **2011**, *365*(1), 85.
[19] V. Vrdoljak, G. Pavlovic, N. Maltar-Strmecki, M. Cindric, *New J. Chem.* **2016**, *40*, 9263.
[20] L. Yang, Y. Juan, L. Yao, H. Wei, H. Shuaidan, W. Dayu, *Inorg. Chem. Commun.* **2018**, *92*, 9.
[21] V. Vrdoljak, G. Pavlovic, T. Hrenar, M. Rubcic, P. Siega, R. Dreos, M. Cindric, *RSC Adv.* **2015**, *5*, 104870.

[22] M. A. Naziri, E. Sahin, N. Seferoglu, B. Shaabani, *J. Coord. Chem.* **2018**, *71*, 89.

[23] R. Gup, C. Gökçe, S. Aktürk, *Spectrochim. Acta A Mol. Biomol. Spectrosc.* **2015**, *134*, 484.

[24] H. Hosseini-Monfared, E. Pousaneh, S. Sadighian, S. W. Ng, E. R. T. Tiekink, *Z. Anorg. Allg. Chem.* **2013**, *639*, 435.

[25] E. Ramachandran, V. Gandin, R. Bertani, P. Sgarbossa, K. Natarajan, N. S. P. Bhuvanesh, A. Venzo, A. Zoleo, A. Glisenti, A. Dolmella, A. Albinati, C. Marzano, *J. Inorg. Biochem.* **2018**, *182*, 18.

[26] D. Matoga, J. Szklarzewicz, W. Nitek, *Polyhedron* **2012**, *36*, 120.

[27] M. Shebl, *J. Mol. Struct.* **2017**, *1128*, 79.

[28] P. P. Netalkar, S. P. Netalkar, S. Budagumpi, V. K. Revankar, *J. Med. Chem.* **2014**, *79*, 47.

[29] H. Farrokhpour, A. Dehbozorgi, M. Manassir, A. N. Chermahini, *J. Mol. Struct.* **2016**, *1107*, 121.

[30] M. Masoudi, M. Behzad, A. Arab, A. Tarahhomi, H. Amiri Rudbari, G. Bruno, *J. Mol. Struct.* **2016**, *1122*, 123.

[31] S. Thalamuthu, B. Annaraj, M. A. Neelakantan, *Spectrochim. Acta A Mol. Biomol. Spectrosc.* **2014**, *118*, 120.

[32] A. H. Kianfar, H. Farrokhpour, P. Dehghani, H. R. Khavasi, *Spectrochim. Acta Part A Mol. Biomol. Spectrosc.* **2015**, *150*, 220.

[33] Y. L. Zhang, W. J. Ruan, X. J. Zhao, H. G. Wang, Z. A. Zhu, *Polyhedron* **2003**, *22*, 1535.

[34] M. Amirnasr, V. Langer, N. Rasouli, M. Salehi, S. Meghdadi, *Can. J. Chem.* **2005**, *83*, 2073.

[35] C. Acilan, B. Cevatemre, Z. Adiguzel, D. Karakas, E. Ulukaya, N. Ribeiro, I. Correia, J. C. Pessoa, *Biochim. Biophys. Acta (BBA)–Gen. Subj.* **2017**, *1861*, 218.

[36] Y. Cui, X. Dong, Y. Li, Z. Li, W. Chen, *Eur. J. Med. Chem.* **2012**, *58*, 323.

[37] L. Jia, H. Cai, J. Xu, H. Zhou, W. Wu, F. Li, Y. Wang, X. Pei, Q. Wang, *Inorg. Chem. Commun.* **2013**, *35*, 16.

[38] B. Mavroidi, M. Sagnou, K. Stamatakis, M. Paravatou-Petsotas, M. Pelecanou, C. Methenitis, *Inorg. Chim. Acta* **2016**, *444*, 63.

[39] C. W. Fong, *Free Radic. Biol. Med.* **2016**, *95*, 216.

[40] S. Y. Ebrahimipour, I. Sheikhshoaie, A. C. Kautz, M. Ameri, H. Pasban-Aliabadi, H. Amiri Rudbari, G. Bruno, C. Janiak, *Polyhedron* **2015**, *93*, 99.

[41] V. Thamilarasan, N. Sengottuvelan, A. Sudha, P. Srinivasan, G. Chakkaravarthi, *J. Photochem. Photobiol. B: Biol.* **2016**, *162*, 558.

[42] M. Anjomshoa, H. Hadadzadeh, S. J. Fatemi, M. Torkzadeh-Mahani, *Spectrochim. Acta Part A Mol. Biomol. Spectrosc.* **2015**, *136*, 205.

[43] X. Zhong, J. Yi, J. Sun, H. L. Wei, W. S. Liu, K. B. Yu, *Eur. J. Med. Chem.* **2006**, *41*, 1090.

[44] P. Tyagi, M. Tyagi, S. Agrawal, S. Chandra, H. Ojha, M. Pathak, *Spectrochim. Acta Part A Mol. Biomol. Spectrosc.* **2017**, *171*, 246.

[45] G. G. Mohamed, E. M. Zayed, A. M. M. Hindy, *Spectrochim. Acta Part A Mol. Biomol. Spectrosc.* **2015**, *145*, 76.

[46] B. S. Creaven, E. Czegledi, M. Devereux, E. A. Enyedy, A. Foltyn-Arfa Kia, D. Karcz, A. Kellett, S. McClean, N. V. Nagy, A. Noble, A. Rockenbauer, T. Szabo-Planka, M. Walsh, *Dalton Trans.* **2010**, *39*, 10854.

[47] S. Y. Ebrahimipour, I. Sheikhshoaie, J. Castro, W. Haase, M. Mohamadi, S. Foro, M. Sheikhshoaie, S. Esmaeili-Mahani, *Inorg. Chim. Acta* **2015**, *430*, 245.

[48] H. W. Huang, *Acta Crystallogr. E: Struct. Rep. Online* **2010**, *66*(12), o3143.

[49] X. Y. Wang, G. B. Cao, T. Yang, *Acta Crystallogr. E Struct. Rep. Online* **2008**, *64*(10), o2022.

[50] G. Ayyannan, P. Veerasamy, M. Mohanraj, G. Raja, A. Manimaran, M. Velusamy, N. Bhuvanesh, R. Nandhakumar, C. Jayabalakrishnan, *Appl. Organomet. Chem.* **2017**, *31*(5), e3599.

[51] Agilent Technologies, *CrysAlis PRO (Version 1.171.39.46)*, Agilent Technologies Ltd **2018**.

[52] G. M. Sheldrick, *Acta Crystallogr.* **2014**, *A71*, 3.

[53] G. M. Sheldrick, *Acta Crystallogr.* **2014**, *C71*, 3.

[54] S. Parvarinezhad, M. Salehi, M. Kubicki, A. Khaleghian, *Appl. Organomet. Chem.* **2021**, *35*, e6443.

[55] S. Parvarinezhad, M. Salehi, R. Eshaghi Malekshah, M. Kubicki, A. Khaleghian, *Appl. Organomet. Chem.* **2022**, e6563.

[56] S. Parvarinezhad, M. Salehi, M. Kubicki, R. Eshaghi Malekshah, *J. Mol. Struct.* **2022**, *1260*, 132780.

[57] A. E. Reed, L. A. Curtiss, F. Weinhold, *Chem. Rev.* **1998**, *88*, 899.

[58] R. F. W. Bader, *Atoms in Molecules, a Quantum Theory*, Oxford University Press, New York, NY **1990**.

[59] M. J. Turner, J. J. McKinnon, S. K. Wolff, D. J. Grimwood, P. R. Spackman, D. Jayatilaka, M. A. Spackman, *CrystalExplorer 17.5*, The University of Western Australia **2017**.

[60] S. Ramezanipoor, S. Parvarinezhad, M. Salehi, A. Grześkiewicz, M. Kubicki, *J. Mol. Struct.* **2022**, *1257*, 132541.

[61] O. Trott, A. J. Olson, *J. Comput. Chem.* **2010**, *31*, 455.

[62] E. F. Pettersen, T. D. Goddard, C. C. Huang, G. S. Couch, D. M. Greenblatt, E. C. Meng, T. E. Ferrin, *J. Comput. Chem.* **2004**, *25*, 1605.

[63] R. Fekri, M. Salehi, A. Asadi, M. Kubicki, *Inorg. Chim. Acta* **2019**, *484*, 245.

[64] R. Fekri, M. Salehi, A. Asadi, M. Kubicki, *Appl. Organomet. Chem.* **2018**, *32*(2), e4019.

[65] R. Fekri, M. Salehi, A. Asadi, M. Kubicki, *Polyhedron* **2017**, *128*(28), 175.

[66] S. Parvarinezhad, M. Salehi, *J. Mol. Struct.* **2020**, *1222*, 128780.

[67] S. Parvarinezhad, M. Salehi, *J. Mol. Struct.* **2021**, *1225*, 129086.

[68] (a) N. Venkatesh, B. Naveen, A. Venugopal, G. Suresh, V. Mahipal, P. Manojkumar, T. Parthasarathy, *J. Mol. Struct.* **2019**, *1196*, 462. (b) L. Y. Xu, Y. M. Chai, C. G. Li, L. Q. Chai, *Appl. Organomet. Chem.* **2021**, *35*(8), 6279.

[69] Y. H. Zhou, X. W. Liu, L. Q. Chen, S. Q. Wang, Y. Cheng, *Polyhedron* **2016**, *117*, 788.

[70] S. Mandal, S. Chatterjee, R. Modak, Y. Sikdar, B. Naskar, S. Goswami, *J. Coord. Chem.* **2014**, *67*, 699.

[71] S. J. Grabowski, *Chem. Rev.* **2011**, *111*, 2597.

[72] A. Ruiz, H. Pérez, C. Morera-Boado, L. Almagro, C. C. P. da Silva, J. Ellena, J. M. García de la Vega, R. Martínez-Álvarez, M. Suárez, N. Martín, *CrstEngComm* **2014**, *16*, 7802.

[73] J. Nawrot-Modranka, E. Nawrot, J. Graczyk, *Eur. J. Med. Chem.* **2006**, *41*, 1301.

[74] W. Sun, P. J. Carroll, D. R. Soprano, D. J. Canney, *Bioorg. Med. Chem. Lett.* **2009**, *19*, 4339.

—WILEY—

[75] M. A. Mansour, A. M. Aboulmagd, H. M. Abdel-Rahman, *RSC Adv.* **2020**, *10*, 34033.

[76] D. A. Milenković, D. S. Dimić, E. H. Avdović, Z. S. Marković, *RSC Adv.* **2020**, *10*, 35099.

[77] J. Haribabu, G. Sabapathi, M. M. Tamizh, C. Balachandran, N. S. Bhuvanesh, P. Venuvanalingam, R. Karvembu, *Organometallics* **2018**, *37*, 1242.

[78] S. Ullrich, C. Nitsche, *Bioorg. Med. Chem. Lett.* **2020**, *30*, 127377.

[79] C. G. Neochoritis, A. Dömling, *Org. Biomol. Chem.* **2014**, *12*(10), 1649.

[80] J. Haribabu, K. Jeyalakshmi, Y. Arun, N. S. P. Bhuvanesh, P. T. Perumal, R. Karvembu, *J. Biol. Inorg. Chem.* **2017**, *22*, 461.

[81] G. M. Sheldrick, *Acta Crystallogr. Sec. A Found Crystallogr.* **2008**, *64*, 112.

[82] J. Haribabu, V. Garisetti, R. Eshaghi Malekshah, S. Srividya, D. Gayathri, N. Bhuvanesh, R. Viswanathan Mangalaraja, C. Echeverria, R. Karvembu, *J. Mol. Struct.* **2022**, *1250*, 131782.

SUPPORTING INFORMATION

Additional supporting information can be found online in the Supporting Information section at the end of this article.